

A Fat Gluino in Disguise

J. REUTER¹^a AND D. WIESLER²^a

^a*DESY Theory Group, Notkestr. 85, D-22603 Hamburg, Germany*

Abstract

In this paper, we investigate how a sizeable width-to-mass ratio for a gluino, as is for example realized in GMSB scenarios, could affect the discovery potential of gluinos at the LHC. More importantly, the influence of the gluino being “fat” on the standard mass and spin determination methods at the LHC are investigated. For this purpose, we focus on gluino production at the LHC, where we do not factorize the first step in the gluino decay cascade, but treat the following decay cascades step in factorization, including full spin correlations. The effects of sizeable width-to-mass ratios from a few up to 15-20 per cent on the endpoint of several mass determination methods as well as on means for discrimination between BSM spin paradigms like SUSY and UED are studied.

¹juergen.reuter@desy.de

²daniel.wiesler@desy.de

1 Introduction and Finite Width Effects

The Standard Model (SM) of particle physics describes all data in the field since today with a very good accuracy. Nevertheless, there are many reasons for physics beyond the SM (BSM), namely the non-existence of a dark matter particle within the SM, the insufficient amount of CP violation to explain the baryon-antibaryon asymmetry in the universe, and the instability of mass terms of fundamental scalar particles against radiative corrections. Supersymmetry has been one of the most favorable candidates to cure these problems. One of its main predictions to be tested best at a hadron collider is the existence of strongly interacting supersymmetric partner particles of the quarks and the gluon, namely squarks and the gluino. Up to now, in the runs at 7 and 8 TeV center-of-mass energy, the Large Hadron Collider (LHC) has not found any traces of supersymmetric particles, which means that these particles cannot be too light. Supersymmetry is part of a large class of BSM models, where new particles around the TeV scale have only weak interactions, like in models with extra dimensions, or Little Higgs models. These kind of models seems to be favored by electroweak precision data, as there are no (big) deviations or inconsistencies in the fit of the electroweak data to the SM. Generically, new particles in weakly interacting models show up as narrow resonances, where in most cases their width is below the detector resolution of the LHC experiments. This is different from strongly interacting scenarios like technicolor, composite Higgs models or conformal sectors where new particles or more like broad resonances (e.g. similar to the ρ resonance) or even similar to continuum-like excitations like in QCD or condensed matter physics.

In the minimal supersymmetric SM (MSSM) and its most simple extensions, all new particles are consequently rather narrow resonances with a width-to-mass ratio, $\gamma := \Gamma/M$, of the order of half a per cent or less. Besides the heavy Higgs bosons in certain parts of parameter space, the gluino \tilde{g} is the only particle that can get a sizeable width-to-mass ratio. In the case, the gluino is heavier than the squarks, there are many decay channels open for the gluino, such that the gluino can easily access a width-to-mass ratio of several, and even up to 15-20 per cent. The theoretical upper limit for this ratio (taking the gluino mass to infinity or equivalently assuming quasi-massless squarks) is 32 per cent. More details under which conditions gluinos can become “fat” are summarized below, when we discuss the model setup for this study.

Since the most severe bottleneck of simulations with multi-particle final states (at least, but not only at tree level) is the integration over the high-dimensional phase space, almost all SUSY studies have been performed with a factorized approach. This is motivated by the fact that a production process of two SUSY particles is followed by subsequent two- or three-body decays. The easiest approximation relies on the narrow-width approximation (NWA) which precisely does this factorization. This can be approved by folding in momentum smearing according to a Breit-Wigner propagator $N(q)/(q^2 - m^2 + im\Gamma)$, where q is the four momentum, m the mass and Γ the width of the associated intermediate particle. In many cases, the most severe effects come from the numerator factor $N(q)$ which depends upon the quantum numbers of the intermediate state, and essentially contains the spin density matrix connecting the production and decay matrix elements. Spin and polarisation information for the intermediate particle are important e.g. in top or W decays, or in BSM physics for the

discrimination between different assignments of particle spins, e.g. between SUSY and UED.

When the decay matrix element (squared) is integrated out, the small width Γ of the intermediate state particle is neglected, as well as the (usually) very small dependence of production and decay matrix elements on the momentum of the intermediate particle q . In a previous study [1] it was shown if one of the five following cases is met, the NWA cannot be applied: (1) the obvious violation, when $\gamma = \Gamma/M$ is not small, e.g. for the ρ resonance in QCD or a corresponding resonance in composite models, (2) if the masses of mother and daughter particle are near-degenerate, $m \sim M$ (decay threshold), e.g. typically in UED, (3) if the mass of the intermediate is close to the kinematical limit of the experiment, $M \sim \sqrt{s}$ (particle threshold), (4) if there are big interferences between different exclusive decay channels (quasi-combinatorial background), and finally (5) if there is a propagator non-separable from the matrix element (e.g. in the case of a non-trivial spectral density of particles or unparticles). In the SM, there are only a few examples where deviations from the NWA really matter, as many (fundamental) particles are relatively narrow (the W with $\gamma = 2.5$ per cent has the largest width-to-mass ratio) in the SM. However, even here sometimes the NWA had to be given up in order to get to predictions that are precise enough to match experimental analyses, e.g. $e^+e^- \rightarrow W^+W^- \rightarrow 4f$ [2]. In general BSM scenarios, such cases appear much more often, cf. e.g. [3,4]. Though there have been systematic improvements of the NWA [5,6] up to the order $\mathcal{O}(\Gamma/M)$, it is always preferable to use full matrix elements for the processes under investigation.

In this paper, we study whether and how much finite-width effects of a heavy gluino do affect its detectability, and its mass and spin determination at the LHC. Sec. 2 defines our benchmark SUSY models, the studied processes and the setup of our simulation. The results are shown in Sec. 3 for the effects of finite widths on the mass determination and in Sec. 4 for the spin determination. Finally, we conclude in Sec. 5.

2 Simulation Setup and Benchmark Model

For the analyses of off-shell effects on endpoint and shape measurements of invariant mass distributions, we assume a SUSY scenario where there are considerable branching ratios of the gluino both into a first- or second-generation squark accompanied by a jet. Furthermore, we assume the presence of a so-called *golden chain* with subsequent decays of the squark into the second-lightest neutralino, which further decays into slepton and lepton, where the slepton then ends up in another lepton and the lightest neutralino. This demands for the specific mass hierarchy in the SUSY particle spectrum, $m_{\tilde{q}_L} > m_{\tilde{\chi}_2} > m_{\tilde{l}_R} > m_{\tilde{\chi}_1}$, which however is not uncommon in phenomenological SUSY models studied in the literature (early cMSSM scenarios such as *SPS1a* [7] inspired the presence of this type of hierarchy). For the study of gluino width effects, we overlay the two main production processes of gluino pair production with the much more abundant – in the case of light(er) squarks – one of associated gluino-squark production:

$$pp \rightarrow \tilde{g}_1 \tilde{g}_2 + X \tag{1}$$

$$pp \rightarrow \tilde{g}_1 \tilde{q}_{L/R} + X \quad . \tag{2}$$

In the first case, Eq. (1)), we take asymmetric decay chains, where one of the two signal gluinos decays into two light (without loss of generality down) quarks and the lightest neutralino, while the other one decays into two bottom quarks and the second-to-lightest neutralino, which further decays via an intermediate (right handed) slepton to two corresponding leptons and a lightest neutralino:

$$\tilde{g}_1 \rightarrow b\tilde{b}_i \rightarrow b\bar{b}\tilde{\chi}_2^0 \rightarrow b\bar{b}l^\pm\tilde{l}_R^\mp \rightarrow b\bar{b}l^\pm l^\mp\tilde{\chi}_1^0 \quad (3)$$

$$\tilde{g}_2 \rightarrow d\tilde{d}_L \rightarrow d\bar{d}\tilde{\chi}_1^0 \quad (4)$$

Notice the index i at the bottom squark owing to the fact, that we include both decay modes of the gluino into \tilde{b}_1 and \tilde{b}_2 . In the second case of squark-gluino associated production (Eq. (2)), we simulate the prompt squark decay into a quark and the lightest neutralino

$$\tilde{q}_{L/R} \rightarrow q\tilde{\chi}_1^0. \quad (5)$$

With the focus on this particular exclusive final state being the same for both production processes we omit additional complications from combinatorial ambiguities. It allows us to study the consequences of off-shell effects without having to suffer from SUSY or combinatorial backgrounds (these have been studied recently in the context of purely hadronic decay modes in [8,11]). Preliminary results on distortions due to off-shell effects have been shown in [9], while distortions of parton-level distributions due to exotic non-standard SUSY particles which could mimic off-shell and combinatorial effects have been studied in [10].

The last decay steps in the cascade of equation, Eq. (3), are particularly well-known: they are identical to the *golden chain* with the replacement of a (first or second generation) squark by a sbottom: $\tilde{q}_L \rightarrow \tilde{b}_i$. This exclusive final state allows for a quite generic study of most of the mass determination methods in the literature [12], while in principle simultaneously reducing combinatorial mis-assignments due to the possibility of b -tagging. Furthermore, in the analysis of off-shell gluino width effects we are able to use methods based on the existence of sbottoms in the cascade.

In the following, we introduce a benchmark scenario that allows for the abovementioned signal decay chain while capturing most of the relevant phenomenological features like a Higgs mass around 125 GeV, heavy colored states beyond the LHC limits [13] and a rich phenomenology of decay patterns. To be as generic as possible, we decided to make use of the phenomenological MSSM with 19 free parameters (p19MSSM), without any high-scale relations among the parameters. All parameters determining the model are given at the electroweak/TeV scale. Their explicit values for the parameter point chosen here are given in Table 1. The mass hierarchy for the decay chain above is valid for this parameter point, and the branching ratios of the four successive two body decay steps are of considerable size:

$$\begin{array}{l} \tilde{g} \rightarrow b\tilde{b}_1 \quad 10 \% \quad \left| \quad \tilde{b}_1 \rightarrow b\tilde{\chi}_2^0 \quad 16 \% \quad \left| \quad \tilde{\chi}_2^0 \rightarrow e^\pm\tilde{e}_R^\mp \quad 42 \% \quad \left| \quad \tilde{e}_R^\pm \rightarrow e^\pm\tilde{\chi}_1^0 \quad 100 \% \right. \right. \\ \tilde{g} \rightarrow b\tilde{b}_2 \quad 07 \% \quad \left| \quad \tilde{b}_2 \rightarrow b\tilde{\chi}_2^0 \quad 34 \% \quad \left| \quad \tilde{\chi}_2^0 \rightarrow \mu^\pm\tilde{\mu}_R^\mp \quad 42 \% \quad \left| \quad \tilde{\mu}_R^\pm \rightarrow \mu^\pm\tilde{\chi}_1^0 \quad 100 \% \right. \right. \end{array}$$

Given these values, the total branching fraction of our exclusive final state from signal gluinos decaying through the benchmark cascade above is roughly 7 %. This number has to be taken with a grain of salt, as the underlying concept of factorized cross sections for exclusive final states into cross sections

M_1	M_2	M_3	A_t	A_b	A_τ	μ	M_A	$m_{\tilde{L}_L}$	$m_{\tilde{L}_R}$
150	250	1200	4000	4000	0	1500	1500	1000	1000
$m_{\tilde{t}_R}$	$m_{\tilde{t}_L}$	$m_{\tilde{q}_L}$	$m_{\tilde{q}_L^3}$	$m_{\tilde{q}_R^u}$	$m_{\tilde{q}_R^d}$	$m_{\tilde{t}_R}$	$m_{\tilde{b}_R}$	$\tan \beta$	
200	1000	1000	1000	1000	1000	4000	1000	10	

Table 1: *Model parameters of the pMSSM parameter point studied in this paper. All numbers (except $\tan \beta$) are in units of GeV.*

times branching ratio as within the NWA might no longer be a good approximation in the presence of off-shell contributions. However, in this study we investigate the effects arising from precisely these kind of contributions far away from the resonant pole of the propagator. A complete treatment should (at least) take into account fully differential four- (or more) particle final states. Since we use these figure merely as rough estimates to determine the actual number of events we expect from our exclusive decay cascade final state, we refrain from such a calculation. All masses of the spectrum were calculated using SOFTSUSY [14], while the particle decay widths were obtained with SUSYHIT [15]. An overview of all model parameters is given in Table 1. Feeding the obtained SLHA file [16,17] for the given mass spectrum into PROSPINO [18], we calculated the relevant cross sections for LHC at 14 TeV: for squark-gluino associated production 376.0 fb, for gluino pair production 47.6 fb, and neutralino-gluino associated production 3.7 fb, respectively. The sum we multiply by the total branching fraction of our exclusive final state (7 %) to arrive at an event number of roughly 9,000 for an overall integrated luminosity of 300 fb^{-1} . Several diluting effects such as detector acceptance, b-tagging efficiencies and event selection criteria may further reduce this figure. For that reason, we took a conservative estimate and chose to analyse an event number of 5,000. The following simulations are based on the most recent version of the event generator WHIZARD [19]. All generated events were exported to HepMC [20] format and afterwards passed through a C++ analysis framework based on ROOT [21], which was specifically developed and tailored to the investigation of deviations from off-shell contributions in spin and mass determination methods.

As we want to investigate effects that come directly from off-shell propagators and interference effects, we compare full matrix-element calculations with factorized approaches in the NWA at parton level, in order to be able to disentangle their effects from pollution that stems from QCD radiation, hadronization and detector effects. To study a “fat” gluino, we use full matrix elements for the production including the first decay of the gluino. More precisely, the first part of Eq. (3) is completely calculated in one step,

$$pp \rightarrow (b\bar{b}\tilde{\chi}_2^0) + (\tilde{g}/\tilde{q}) \quad , \quad (6)$$

including all interferences. On the other hand, the successive decays of the second-to-lightest neutralino and the “spectator” gluino or squark are factorised with full spin correlations using the NWA. Furthermore, the phenomenological width-to-mass ratio $\gamma = \Gamma/M$ is scanned over the following values

$$\gamma \in \{0.5\%, 2.5\%, 5.0\%, 10.0\%, 15.0\%, 20\%, 25\%\}. \quad (7)$$

This set is chosen so as to resemble a broad range of possible widths that might be realised in nature. While the lowest value is a typical width for standard parameter points, values above 10 % appear when the gluino is clearly heavier than the squarks as in GMSB setups. There is also a particular phenomenological reasoning behind the range of values, which will be discussed at the beginning of the next section. Using this relative width ratio γ we study the impact of off-shell contributions on a selected choice of mass and spin determination methods listed in the next two sections.

3 Effects on Mass Measurements

We begin our investigation with the study of several mass measurement variables. A large width Γ in the gluino propagator affects the momenta of both the intermediate sbottom and the near (bottom) quark b_n , as both are directly resulting out of the gluino propagator. The far bottom quark b_f , coming from the sbottom decay, on the other hand is expected to receive only a minor modification and thus should not be part of distorted invariant mass distributions. Fig. 1 depicts the transverse momentum distributions of both the near and the far bottom quark and their distortion with respect due to different values of γ . The black (solid), red (short-dashed), green (dotted), blue (short-dashed-dotted), yellow (long-dashed-dotted), magenta (long-dashed-double-dotted) and cyan (long-dashed) line correspond to $\gamma = 0.5 \%$, 2.5% , 5.0% , 10.0% , 15.0% , 20.0% and 25.0% , respectively. As expected, the far bottom quark, is almost unaffected by a fat gluino as it originates from the subsequent decay of the sbottom. On the other hand, we observe that the near bottom quark exhibits a considerable distortion in its p_T distributions, already visible by eye. While there is an obvious tendency for a severely increasing distortion within the first five values of γ (up to 15 %), the two largest effective widths (20 and 25 %) exhibit only a slight further increase. These values are anyhow to some extent academic, since in realistic scenarios they are quite hard to realize: either these scenarios are already excluded due to the Higgs boson discovery at 125 GeV, or the gluinos are so heavy that they are out of reach of a 14 TeV LHC. In the first plot for the transverse momentum distributions, we included them to illustrate the effect of a moderate saturation. This observation motivates us to leave out the two highest values $\gamma = 20.0\%$, 25.0% and from now on investigate the reduced range of values up to 15 %, also in order not to make the plots too crowded.

As the far quark/jet is (almost) not affected by the off-shell effects, we restrict our investigation to that subset of mass determination observables introduced in [12] that contain the near quark b_n : $\{m_{bb}, m_{b_n\ell,low}, m_{b_n\ell,high}, m_{bb\ell,low}, m_{bb\ell,high}, m_{b_n\ell\ell}, m_{bb\ell\ell}\}$. These are the invariant mass distributions of either two b jets, one b jet and a lepton (with the softer or the harder jet, respectively), of two b s with a lepton, or finally two jets and two leptons. All these variables are tailor-made for exclusive decay cascades, which are shown in the next subsection, while the subsection after that shows the effect of broad gluinos on inclusive variables (like e.g. M_{T_2}).

3.1 Exclusive Cascades

$\boxed{m_{bb}}$ The first mass edge we study is the classical dijet endpoint of the first gluino decay step. Due to the scalar propagator of the intermediate bottom squark, we expect to see no effects of spin

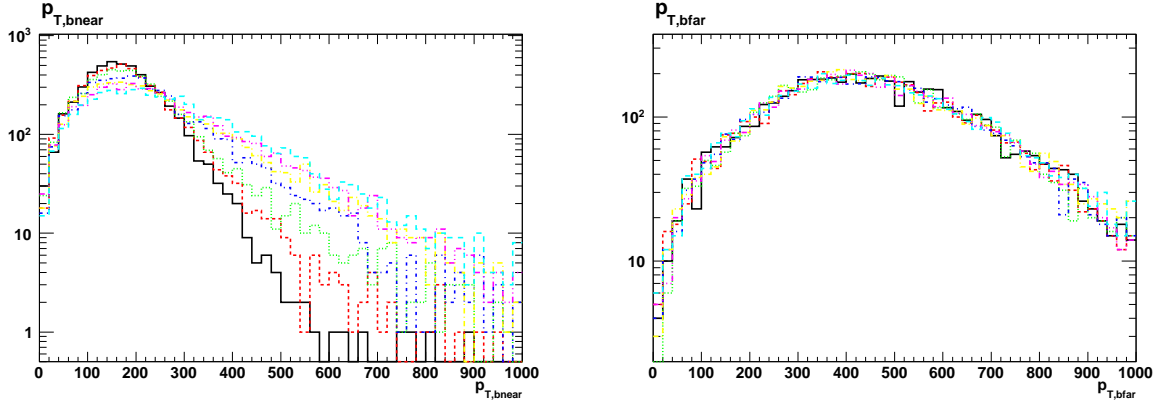


Figure 1: *Transverse momentum distributions of the two bottom quarks in the signal cascade (near from the gluino and far from the sbottom decay). The black (solid), red (short-dashed), green (dotted), blue (short-dashed-dotted), yellow (long-dashed-dotted), magenta (long-dashed-double-dotted) and cyan (long-dashed) line correspond to $\gamma = 0.5\%$, 2.5% , 5.0% , 10.0% , 15.0% , 20.0% and 25.0% , respectively.*

correlation, such that the shape of the distribution should resemble the well-known triangular nature of the di-lepton edge with a linear rise from 0 to m_{bb}^{\max} , where a sharp cutoff marks the endpoint. Figure 2 shows on the left hand side the simulated distributions for five different values of γ , where

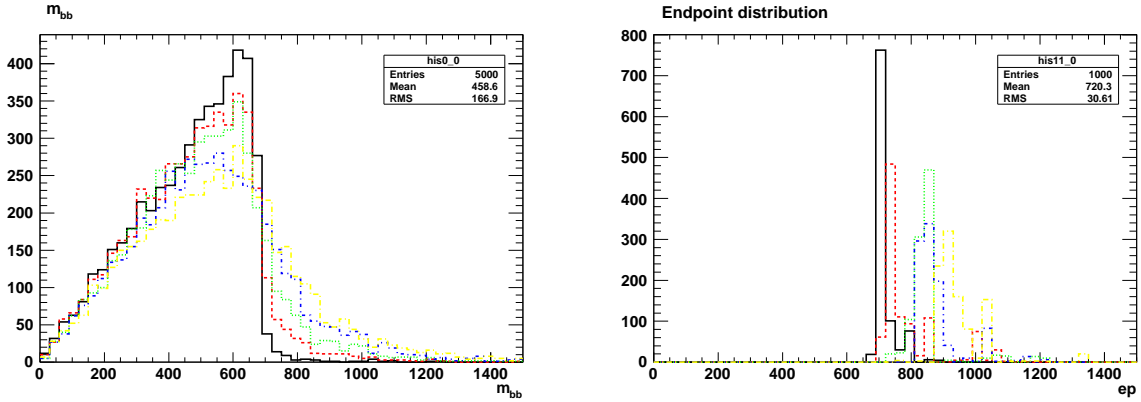


Figure 2: *Left hand side: Invariant dijet mass of two bottom quarks, m_{bb} , from the gluino decay for different values of γ (line styles identical to Fig. 1). On the right hand side, the distribution of endpoints obtained as fit parameters of the edge-to-bump method.*

the line colors are identical to Fig. 1. One notices that the solid black line deviates only very little from the ideal triangular shape dictated by phase space (one basically has a small smearing at the edge of the distribution), which is a direct consequence of the relatively small width: $\Gamma = 0.005 M$. The situation drastically changes when the width is incrementally increased: the distortion steadily grows and starts to wash out the clear-cut edge structure with increasing γ . At high values of γ ($\geq 5\%$) the distribution acquires an irreducible tail, which mimics other distorting effects such as combinatorial mis-assignments or detector smearing already at this early parton level stage. However, we want to

stress the fact, that this kind of deviation from off-shell contributions is irreducible in the sense, that it cannot be tuned away e.g. by other methods designed to minimize combinatorial problems.

In the next step, it is our goal to quantify these intrinsic contributions by estimating the distortion of the shape in the vicinity of the endpoint as a function of the effective width-to-mass ratio γ . For this study, we use the edge-to-bump method [22]. It translates the human bias in fitting different lines to kinematical distribution and hence a systematic uncertainty into a statistical uncertainty over a sample of line/edge fit, thereby scanning of a variety of different fit ranges. It allows us to extract the edge information and to discriminate different endpoint behaviours in an unbiased way. In a nutshell, the approach fits a naive linear kink function \mathcal{O} (1000) times and returns bumps at the most likely positions of inks (supposedly physical edges) in the original distribution.

As a first estimate of the impact of width effects on the measurement, we consider the shift of the actual endpoint position with respect to the value of γ . Table 2 discloses in the second column these values obtained with our own implementation of the method described in detail in [9]. The according distributions are in Fig. 2 on the right hand side. While for small width-to-mass ratios of 0.5% the obtained value (708 GeV) is close to the template one (679.6 GeV), the endpoint positions for large of γ are off by more than 200 GeV (920 GeV), using the same method and settings.

An alternative, but related measure for the endpoint smearing is given by the size of the corresponding error estimates. Their increase with respect to γ reflects the observation that the spread of endpoint values in the right plot of Fig. 2 is considerably enhanced for an increased effective width. While for $\gamma = 0.5\%$ the purely statistical error is small, the sheer growth of the standard deviation going up to $\gamma = 15.0\%$ by nearly two orders of magnitude serves as another good indication for a huge endpoint smearing. This raises an important point: the overly high confidence expressed through the small errors of endpoints for low values of γ is a mere binning effect and does not represent a realistic error estimate for sophisticated endpoint measurements. Moreover, these error estimates of the edge-to-bump method are purely statistical and reflect the transformation of a statistical uncertainty on an endpoint position onto the particular position of a mean value in a distribution of fit results. Since the binning of a histogram is bounded by experimental resolutions, a relatively large minimum bin size results in a systematic underestimation of the given errors.

The usage of the endpoint position as a measure for distortion is based on just one fit parameter (the so-called p_4 , for details cf. [22,9]) of the edge-to-bump method. A detailed observation of the edge fitting function suggests to make use of the sampling point parameters p_2 and p_3 , which are the two linear slopes left and right of a possible edge or kink. Notwithstanding the fact, that the off-shell contributions tend to wash out the sharp edge and lead to smoother and longer tails, we propose to use the absolute difference of the two slopes as well as the ratio of the two slope parameters as measures to quantify the amount of edge distortion:

$$s_d := |p_3 - p_2| \tag{8}$$

$$s_r := |p_2/p_3| \tag{9}$$

For each edge fit, both values are calculated from the parameters returned by the edge-to-bump method. Ideally, for a pure phase space distribution of triangular shape and no smearing beyond the

sharp cutoff, the first slope is infinite and the second slope zero, hence the slope difference maximal (namely infinite) and the slope ratio minimal (namely zero). In that sense, the difference in slopes measures the sharpness of a kink in the distribution whereas the ratio returns information about the size of the second slope relative to the first one (pronouncedness of the kink). A ratio close to zero may thus be attributed to a tail-less distribution such as the triangular shaped one. Keep in mind, that due to the sanity checks of our method, $|p_2| < |p_3|$ and hence $s_r \in (0, 1)$. The full treatment of large width effects on the other hand introduces a tail and smears the endpoint behavior, which gives rise to considerably smaller slope differences and higher slope ratios. If the returned fit value of such a slope difference is compatible with zero, the underlying distribution apparently lacks robust kinky features. Extraction of such shallow endpoints is therefore a very delicate task.

In the last two columns of Tab. 2 we collect results for the slope differences and slope ratios of the invariant di-bottom mass for all five scan values of γ . In Fig. 3 we show the impact of the different values of γ : while we observe slope differences well above one and small slope ratios compatible with zero for small γ , at an effective width of already 5 % the mean \bar{s}_d is reduced to a value smaller than one. The slope ratio exhibits an equivalent behavior: the mean value \bar{s}_d is increased by a factor of 10.

γ [%]	\bar{m}_{bb}^{\max}	\bar{s}_d	\bar{s}_r
0.5	708.5 ± 0.9	5.70 ± 2.90	0.014 ± 0.008
2.5	740.9 ± 2.5	1.71 ± 1.17	0.064 ± 0.028
5.0	835.7 ± 19.2	0.78 ± 0.24	0.084 ± 0.023
10.0	886.5 ± 13.0	0.67 ± 0.08	0.141 ± 0.045
15.0	921.3 ± 25.9	0.62 ± 0.04	0.131 ± 0.035

Table 2: Adapted mean values of endpoint positions (in GeV), slope differences (in 1/GeV) and slope ratios for invariant di-bottom mass m_{bb} .

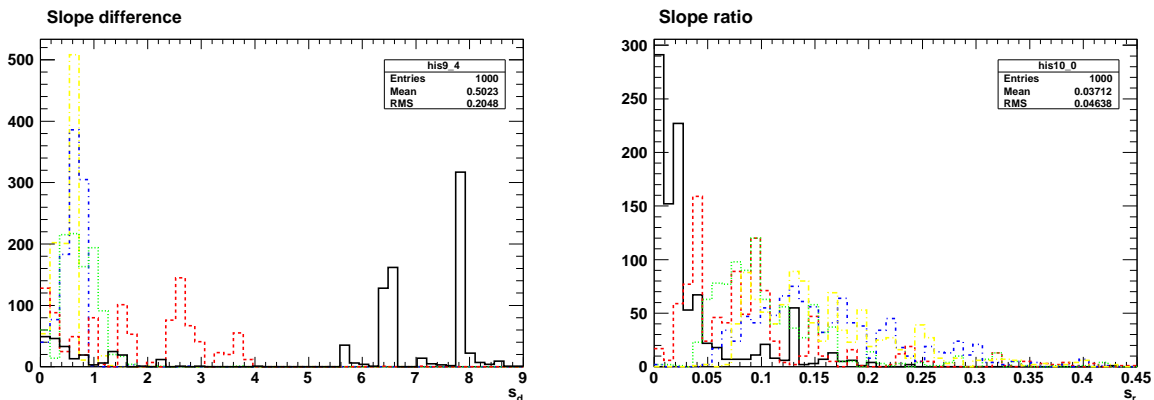


Figure 3: Statistically distributed slope differences (left) and ratios (right) for the dijet invariant mass m_{bb} obtained as fit parameters with the edge-to-bump method.

$m_{b_n \ell}$ Next, we investigate the mass edges obtained by the minimization and maximization over two possible lepton combinations with the near bottom quark. Their definitions are:

$$m_{b_n \ell, low} = \min [m_{b_n \ell^+}, m_{b_n \ell^-}] \quad (10)$$

$$m_{b_n \ell, high} = \max [m_{b_n \ell^+}, m_{b_n \ell^-}] \quad , \quad (11)$$

while their endpoints given are given by

$$(m_{b_n \ell_{low}}^{\max})^2 = \min [(m_{b_n \ell_n}^{\max})^2, (m_{b_n \ell_{eq}}^{\max})^2] \quad (12)$$

$$(m_{b_n \ell_{high}}^{\max})^2 = \max [(m_{b_n \ell_{eq}}^{\max})^2, (m_{b_n \ell_f}^{\max})^2] \quad (13)$$

with

$$(m_{b_n \ell_{eq}}^{\max})^2 = \frac{(m_g^2 - m_b^2)(m_\ell^2 - m_{\tilde{\chi}_1^0}^2)}{(2m_\ell^2 - m_{\tilde{\chi}_1^2}^2)} .$$

By the very nature of the intermediate particles, there is a small correlation of the leptons and the

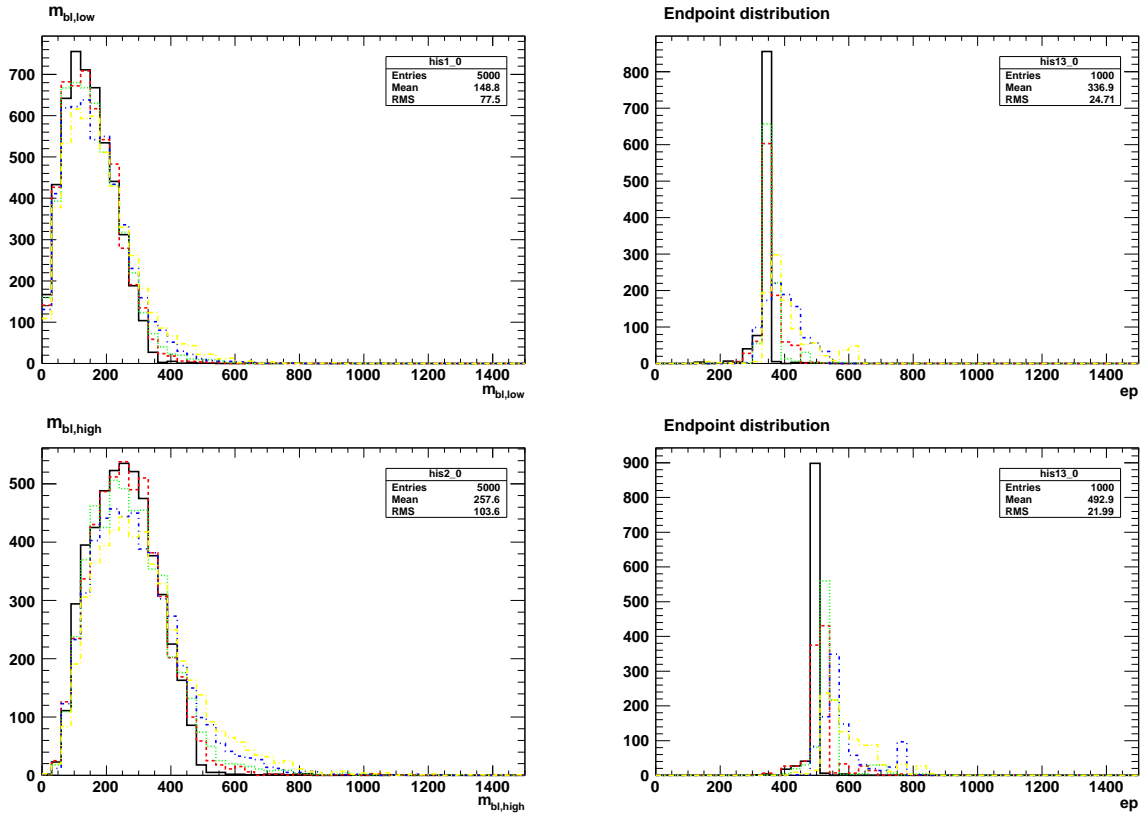


Figure 4: Left: Invariant mass of near bottom quark and lepton as a function of $m_{bl,low}$ (upper plot) and $m_{bl,high}$ (lower plot) for different values of γ . The black (solid), red (short-dashed), green (dotted), blue (short-dashed-dotted), and yellow (long-dashed-dotted) correspond to $\gamma = 0.5 \%$, 2.5% , 5.0% , 10.0% , and 15.0% , respectively. Right: Distribution of the corresponding endpoints obtained as fit parameters with the edge-to-bump method for $m_{bl,low}$ (upper plot) and $m_{bl,high}$ (lower plot).

bottom quark, that manifests itself in the shape of the distributions. Hence, with no pure phase

space shape, we expect the distortion to be less pronounced in comparison to the invariant di-bottom mass. Especially $m_{b_{n\ell},low}$ should not contain too much excess events in the upper parts, since these contributions will mostly be omitted due to the minimization procedure. The variable $m_{b_{n\ell},high}$, on the other hand, will severely be affected for the very same reason. The distributions in Fig. 4 on the left hand side (upper and lower plot) confirm these conjectures. The extracted endpoints depicted on the corresponding right hand sides of the upper and lower line in Fig. 4 and their numerical values in Table 3 also support this statement: while for $m_{b_{n\ell},low}$ the overall endpoint variation with respect to γ is about 40 GeV, $m_{b_{n\ell},high}$ suffers from more than twice the endpoint shift with a value of about 80 GeV. Comparing this to the expected ideal edge positions

$$m_{b_{n\ell},low}^{\max} = 364.4 \text{ GeV} \quad (14)$$

$$m_{b_{n\ell},high}^{\max} = 493.1 \text{ GeV} \quad (15)$$

calculated from Eq. (11), we find that the discrepancy for $m_{b_{n\ell},low}$ is indeed small, and the determined value is mostly in agreement with the expectation. For $m_{b_{n\ell},high}$, however, the endpoint shift is as large as 15%. The adapted slope differences \bar{s}_d show a similar picture: while the numbers of

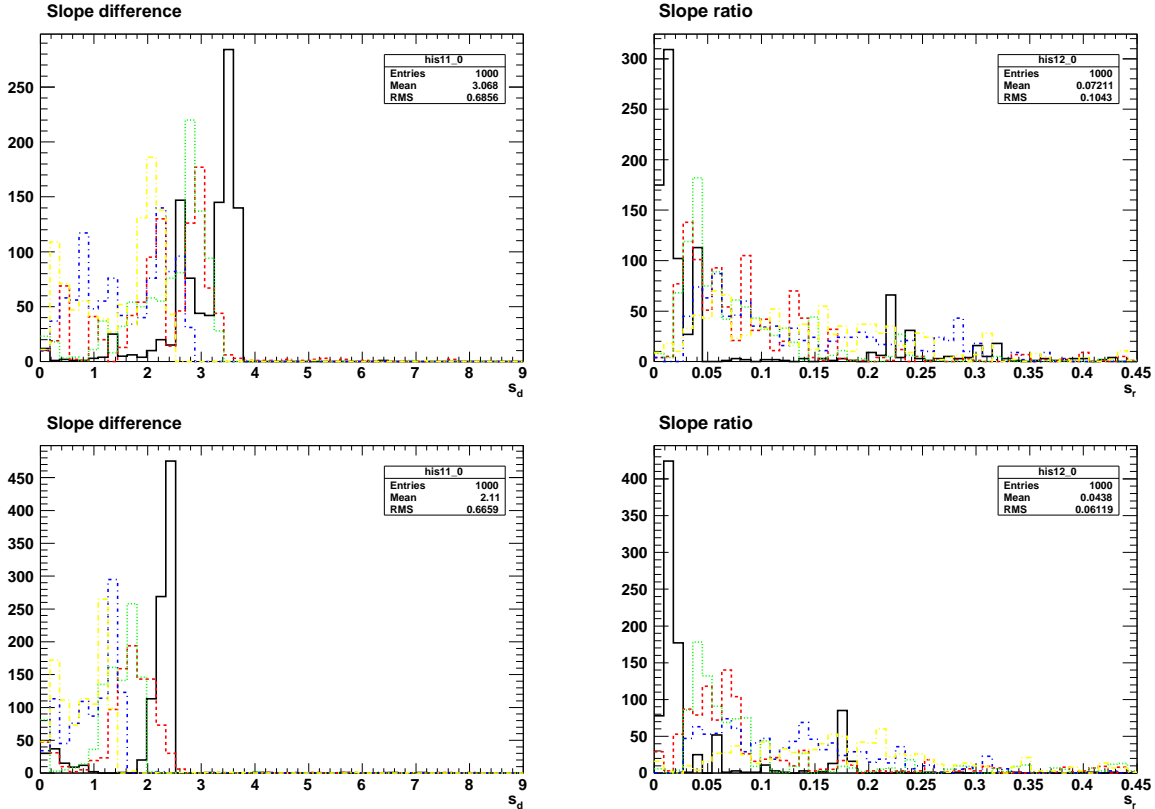


Figure 5: Statistically distributed slope differences (left) and slope ratios (right) for $m_{bl,low}$ (upper plot) and $m_{bl,high}$ (lower plot), obtained as fit parameters by means of the edge-to-bump method.

the minimized distributions exhibit only a mild overall decline, the maximized version illustrates an apparent tendency of \bar{s}_d to decrease with rising γ . As for the slope ratios \bar{s}_r , the same holds, but to

an even greater extent, in that for $m_{bl,low}$ the three intermediate ratios are all in the same ballpark, whereas for $m_{bl,high}$, \bar{s}_r increases by nearly one order of magnitude.

γ [%]	$\bar{m}_{bl,low}^{\max}$	\bar{s}_d	\bar{s}_r	$\bar{m}_{bl,high}^{\max}$	\bar{s}_d	\bar{s}_r
0.5	341.4 ± 6.7	3.25 ± 0.38	0.014 ± 0.007	499.8 ± 0.3	2.35 ± 0.03	0.017 ± 0.005
2.5	356.6 ± 2.7	2.58 ± 0.47	0.055 ± 0.025	511.2 ± 3.6	1.80 ± 0.26	0.055 ± 0.018
5.0	355.5 ± 1.8	2.82 ± 0.25	0.041 ± 0.011	527.0 ± 11.9	1.55 ± 0.25	0.054 ± 0.017
10.0	383.0 ± 39.6	1.59 ± 0.77	0.066 ± 0.024	556.3 ± 13.4	1.00 ± 0.44	0.103 ± 0.048
15.0	377.2 ± 22.3	1.47 ± 0.74	0.124 ± 0.069	579.0 ± 47.9	0.79 ± 0.40	0.158 ± 0.059

Table 3: Adapted mean values of endpoint positions (in GeV), slope differences (in $1/\text{GeV}$) and slope ratios for $m_{bl,low}$ and $m_{bl,high}$, respectively.

m_{bbl} Extending the *low*- and *high*-type invariant masses from above by the additional (far) bottom quark, we arrive at a three-particle invariant mass, that has a similar feature as the ones just discussed: an intermediate neutralino propagator communicating spin correlations and allowing for a similarly altered shape compared to the triangular phase space. If we now start to gradually increase the effective width parameter γ , the off-shell contributions start to enter the game in a more severe way as for the two-particle invariant masses, $m_{bl,low}$ and $m_{bl,high}$. This can be understood in terms of the inclusion of nearest neighbors: since the invariant di-bottom mass is heavily distorted by width effects, and it is always included in both $m_{bbl,low}$ and $m_{bbl,high}$, we in fact expect to observe large deviations. In that sense – and in contrast to $m_{bl,low}$ – the minimization procedure over two possible lepton combinations is not able to suppress the appearance of these intrinsic contributions, as can be seen in Fig. 6. Regarding the shift of edge positions, the situation is comparable to the case of m_{bb} : both $m_{bbl,low}$ and $m_{bbl,high}$ exhibit displacements of up to 150 and 180 GeV, respectively. For the highest value of $\gamma = 0.15$ in Table 4, we notice an exceptionally small error estimate for the endpoint position of $m_{bbl,low}$ in contrast to an unusually large one for $m_{bbl,high}$. The reasoning behind this is a trivial matter of statistics as is evident from Figure 6: while the lower of the two invariant masses has a sharp drop at the bin corresponding to the endpoint position, the higher distribution has two such *fake* kinks at around 1100 and 1250 GeV, respectively. These are purely statistical issues happening by chance and attributed to the low overall number of events of 5,000. Hence the gross under- and overestimation of the error estimates for both edges. The mean value however still captures the important feature of endpoint translation: a shift of the returned mean value of the edge-to-bump method of up to 180 GeV. Comparing these with the theoretically expected values

$$m_{bbl,low}^{\max} = 868.6 \tag{16}$$

$$m_{bbl,high}^{\max} = 996.6 \tag{17}$$

we again find agreement for small widths, but large deviations for high values of γ . In Fig. 7 and Table 4, the slope differences \bar{s}_d (ratios \bar{s}_r) of the two variables both display a clear decreasing (increas-

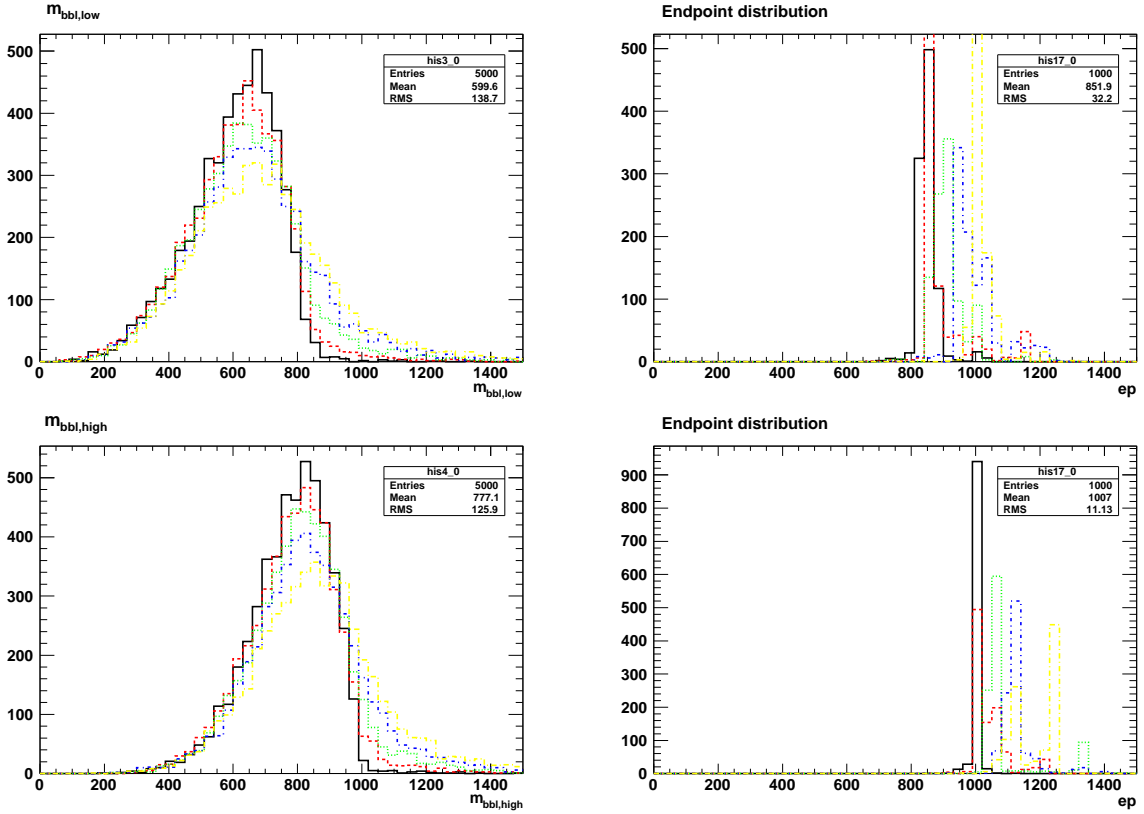


Figure 6: *Left: Invariant mass of near bottom quark and leptons, varied as defined by $m_{bb,low}$ (top) and $m_{bb,high}$ (bottom) for different values of γ (line style identical to Fig. 4). Right: Distribution of the corresponding endpoints obtained as fit parameters with the edge-to-bump method for $m_{bb,low}$ (top) and $m_{bb,high}$ (bottom).*

γ [%]	$\bar{m}_{bb,low}^{\max}$	\bar{s}_d	\bar{s}_r	$\bar{m}_{bb,high}^{\max}$	\bar{s}_d	\bar{s}_r
0.5	845.2 ± 11.6	2.87 ± 0.50	0.025 ± 0.011	1009.7 ± 00.4	3.47 ± 0.10	0.009 ± 0.005
2.5	864.4 ± 02.2	1.79 ± 0.91	0.046 ± 0.020	1017.0 ± 01.7	2.11 ± 0.77	0.041 ± 0.012
5.0	900.8 ± 23.5	1.45 ± 0.22	0.067 ± 0.022	1060.0 ± 10.6	1.72 ± 0.32	0.050 ± 0.012
10.0	979.4 ± 34.8	0.62 ± 0.29	0.156 ± 0.051	1120.8 ± 11.3	0.94 ± 0.22	0.126 ± 0.031
15.0	1002.3 ± 4.9	0.71 ± 0.07	0.163 ± 0.041	1184.3 ± 62.9	0.63 ± 0.30	0.175 ± 0.052

Table 4: *Adapted mean values of endpoint positions (in GeV), slope differences (in 1/GeV) and slope ratios for $m_{bb,low}$ and $m_{bb,high}$.*

ing) trend for growing (falling) effective width factors γ and thus confirm our choice as a parameter quantifying the size of the off-shell effects on the quality of the mass determination.

$m_{b_n\ell\ell}$ The last three-particle invariant mass we investigate is the combination of the near bottom quark and the lepton pair. Without the particular need for distinction between the two leptons, we expect to observe only a moderate distortion for large gluino widths, which might be weakened by

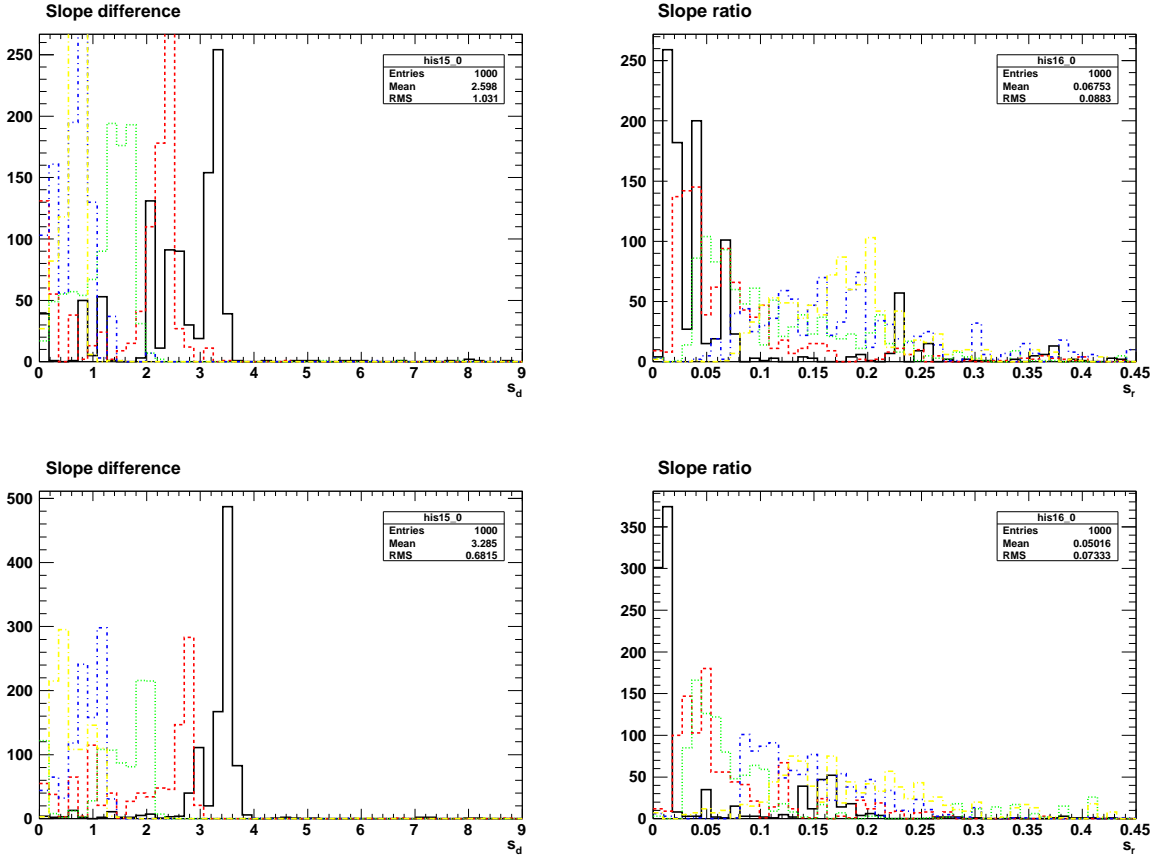


Figure 7: *Statistically distributed slope differences (left) and slope ratios (right) for $m_{bbll,low}$ (top) and $m_{bbll,high}$ (bottom), obtained as fit parameters of the edge-to-bump method.*

the fact that the first linear slope of the undistorted distribution is not maximally steep since $m_{b_n ll}$ is not built out of direct next neighbors in the decay chain. An example of a maximally steep endpoint behavior is the undistorted invariant di-bottom mass, whose first slope parameter would ideally be infinite due to the triangular (phase-space) shape. Fig. 8 depict in the upper line $m_{b_n ll}$ and the corresponding endpoint distributions, numerical values of which are given on the left-hand side of Table 5. Despite a fairly accurate endpoint estimate for up to $\gamma = 2.5\%$ (in comparison with the theoretical value of 578.8 GeV), there is still a deviation of substantial size for large widths of up to 100 GeV. The two slope parameters both behave similarly to what we have already seen with other invariant mass variables (cf. Fig. 9): an average slope difference \bar{s}_d of well above two is reduced to a value below one, that is compatible with zero within two standard deviations. For small widths, the slope ratio \bar{s}_r is also close to zero, but increasing γ results in a steady growth of \bar{s}_r of more than one order of magnitude in size to values of up to 16 %.

m_{bbll} Combining all objects from one cascade, we obtain the variable m_{bbll} , which has a very clear-cut endpoint and a steep edge structure, since it is constructed out of next neighbors only. The sharper the drop of the distribution at the vicinity of the edge, the larger we expect the impact of

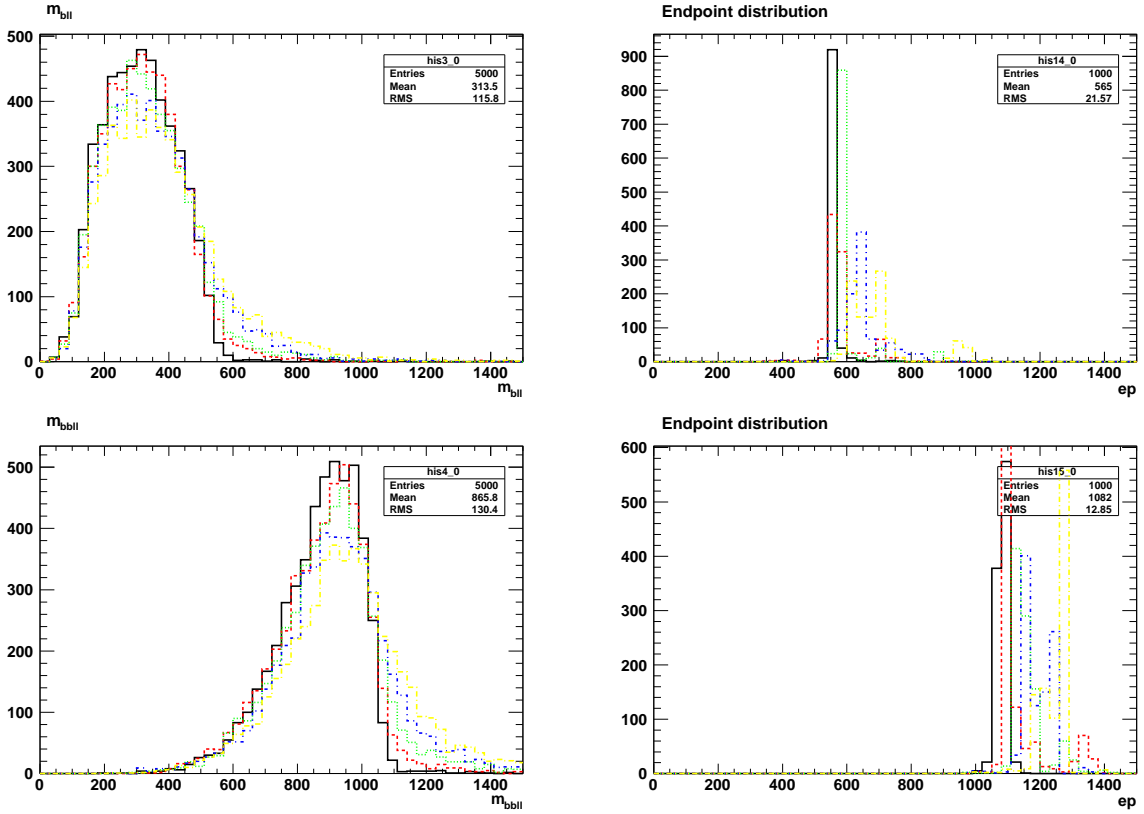


Figure 8: *Left: Invariant mass of bottom quark(s) and leptons: $m_{b_n\ell\ell}$ (top) and $m_{bb\ell\ell}$ (bottom) for different values of γ . The black (solid), red (short-dashed), green (dotted), blue (short-dashed-dotted), and yellow (long-dashed-dotted) correspond to $\gamma = 0.5\%$, 2.5% , 5.0% , 10.0% , and 15.0% , respectively. Right: Distribution of the corresponding endpoints obtained as fit parameters of the edge-to-bump method for $m_{b_n\ell\ell}$ (top) and $m_{bb\ell\ell}$ (bottom).*

off-shell contributions to be, even so if just one out of four propagators, in our case the signal gluino, is affected. From the lower line of Fig. 8, the amount of distortion is already visible by eye. A more quantitative statement is given in terms of numerical values on the right-hand side of Table 5. While the estimated endpoints for small values of γ are in gross agreement with the theoretically expected value of 1092.7 GeV, the largest deviation of $m_{bb\ell\ell}^{\max}$ for $\gamma = 15\%$ is up to 172 GeV. A similar picture as for $m_{b_n\ell\ell}$ is found for the slope parameters (cf. also Fig. 9): ranging from just below five down to well below one, the slope difference exhibits an even larger spread of values. The slope ratios on one hand are compatible with zero for the smallest width $\gamma = 0.5\%$, but, on the other hand, increase by a factor of 15 for the largest off-shell contribution.

3.2 Inclusive Approaches

Up to now, we only studied exclusive invariant mass variables, i.e. combinations of objects arising from one cascade side from a decay of just one single mother. In our case, this was taken to be the gluino, which has a large variety of possible decay patterns and consequently a plethora of interesting invariant mass combinations. Restricting the analysis to just one particular decay cascade entails

γ [%]	\bar{m}_{bll}^{\max}	\bar{s}_d	\bar{s}_r	\bar{m}_{bbll}^{\max}	\bar{s}_d	\bar{s}_r
0.5	565.4 ± 1.7	2.37 ± 0.15	0.010 ± 0.002	1079.3 ± 2.4	4.64 ± 0.51	0.011 ± 0.009
2.5	568.5 ± 3.4	1.92 ± 0.08	0.080 ± 0.037	1105.1 ± 1.3	2.22 ± 1.22	0.035 ± 0.013
5.0	594.5 ± 2.0	1.56 ± 0.04	0.050 ± 0.012	1150.2 ± 19.9	1.34 ± 0.70	0.078 ± 0.020
10.0	640.0 ± 12.0	0.94 ± 0.25	0.142 ± 0.064	1193.7 ± 37.4	1.00 ± 0.44	0.163 ± 0.041
15.0	668.6 ± 40.5	0.65 ± 0.33	0.157 ± 0.050	1251.2 ± 30.9	0.78 ± 0.17	0.182 ± 0.036

Table 5: Adapted mean values of endpoint positions (in GeV), slope differences (in $1/\text{GeV}$) and slope ratios for m_{bll} and m_{bbll} .

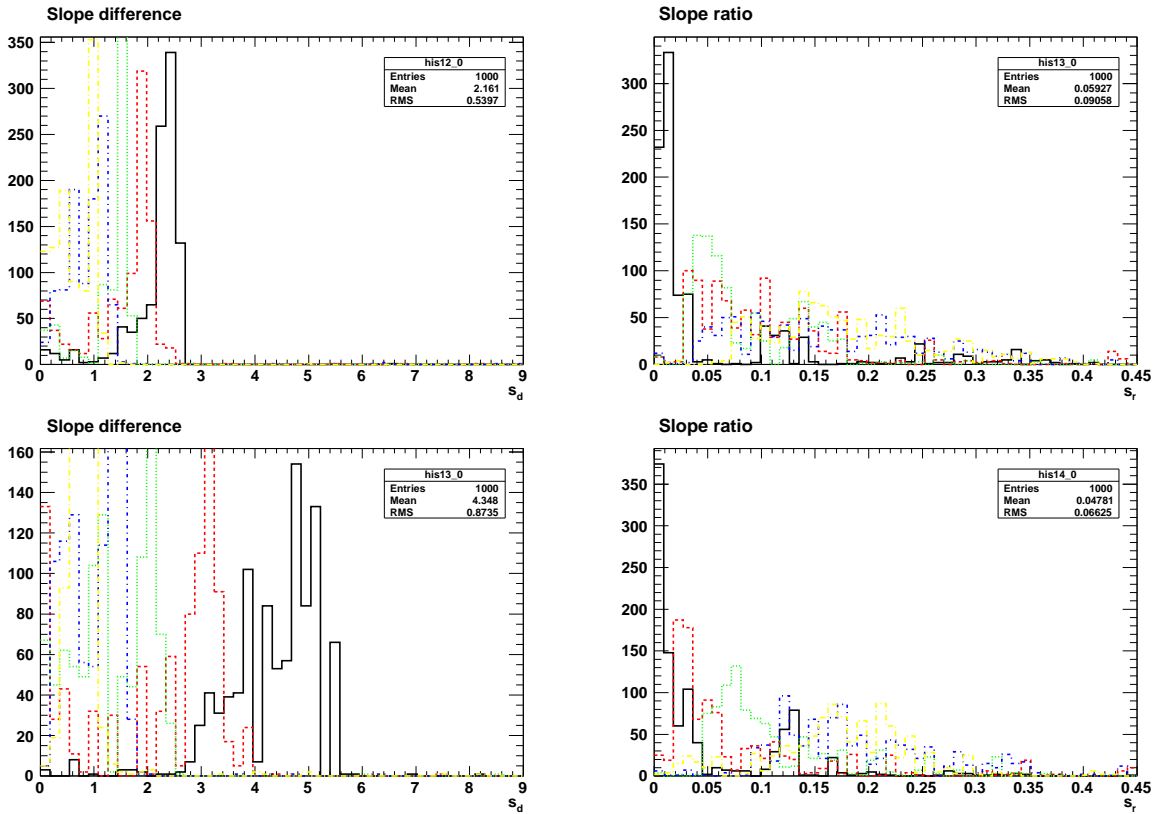


Figure 9: Statistically distributed slope differences (left) and ratios (right) for m_{bll} (top) and m_{bbll} (bottom) obtained as fit parameters of the edge-to-bump method.

several problems, the largest is presumably combinatorics. Consider for example the symmetric case of two identical decay chains of the type we have analyzed so far, where not one, but two gluinos decay into two bottom quarks, two leptons and the lightest neutralino. All variables we have just discussed assume that a differentiation between the two cascades is somehow given (e.g. the partitioning of four leptons into 2×2 leptons). However, a priori, there is no general recipe that always allows for such a correct assignment. This severely affects the usability of these exclusive variables and is known as the combinatorial problem.

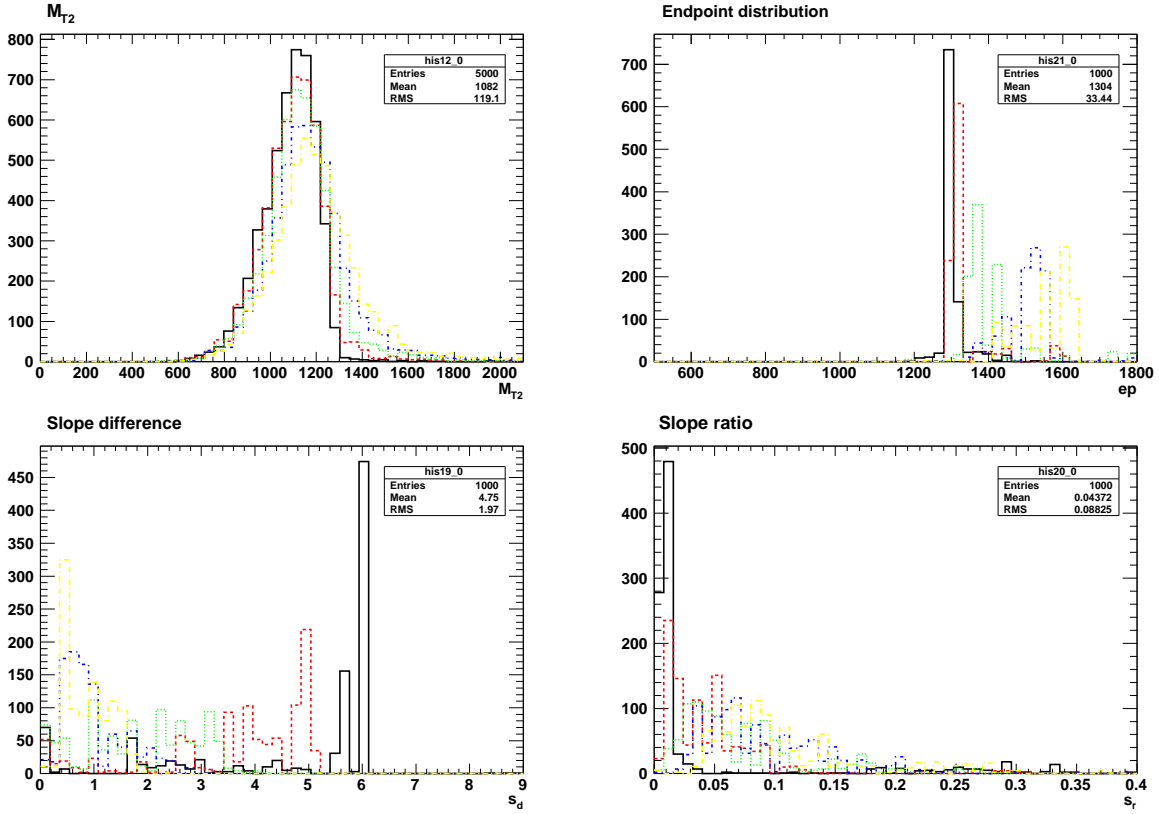


Figure 10: M_{T2} distribution (upper left) and its statistically distributed endpoints (upper right), slope differences (lower left) and slope ratios (lower right) obtained as fit parameters of the edge-to-bump method for five different values of γ . The color scheme is the same as in Fig. 8.

M_{T2} An alternative, less exclusive approach is M_{T2} as introduced in [23], which is a grouping of the measured objects into two subsets and a following minimization procedure over the invariant transverse masses. Although M_{T2} is similarly affected by the combinatorial problem (since here the visible momentum has to be split into two separate sides as well) there are methods which address this issue¹. In the remainder of this chapter we circumvent these kind of combinatorics through two non-identical decay chains, which allow us to directly concentrate on the off-shell effects. Hence, the partition of visible momenta into two sides for the application of $M_{T2}(p_{vis}^{(1)}, p_{vis}^{(2)}, \cancel{p}_T, m_\chi)$ is trivially given by

$$p_{vis}^{(1)} = \{b, \bar{b}, \ell^\pm, \ell^\mp\} \quad (18)$$

$$p_{vis}^{(2)} = \{q, \bar{q}\} \quad , \quad (19)$$

where the light-flavor partonic jets are assigned to one side and the remaining objects to the other. The input test mass of the invisible sparticle was set to $m_\chi = 150$ GeV close to the true value of the benchmark scenario. Figure 10 illustrates in the upper left plot the impact of the effective width parameter γ on the distribution of M_{T2} : similar to the exclusive invariant mass variables

¹e.g. M_{TGen} [24], which is the minimum of M_{T2} for all possible momentum assignments into two partitions

discussed above, relative widths larger than 2.5 % result in substantial smearing and a long tail in the distributions, which is absent at lower values. Owing to the general minimization procedure of M_{T2} , the effect is somewhat smaller than for exclusive variables such as m_{bb} or $m_{bb\ell\ell}$, which is underlined by the numerical results given in Table 6. The endpoint M_{T2}^{\max} is given by the parent sparticle mass,

γ [%]	\bar{M}_{T2}^{\max}	\bar{s}_d	\bar{s}_r
0.5	1293.7 ± 0.8	5.92 ± 0.21	0.009 ± 0.003
2.5	1315.0 ± 10.8	4.42 ± 0.54	0.029 ± 0.017
5.0	1381.0 ± 27.4	1.82 ± 1.03	0.054 ± 0.027
10.0	1526.0 ± 18.6	0.70 ± 0.20	0.072 ± 0.029
15.0	1589.5 ± 31.4	0.87 ± 0.40	0.079 ± 0.022

Table 6: Adapted mean values of endpoint positions (in GeV), slope differences (in 1/GeV) and slope ratios for M_{T2} .

thus we expect to observe a clear edge structure at the gluino mass of 1277 GeV. Up to a slight overshoot, this is in gross agreement with the values given for $\gamma < 5\%$. However, effective widths of up to 15 % lead to an edge shift of nearly 300 GeV. This is the largest translation of an endpoint we have obtained so far and can be understood in terms of the underlying topology: in this inclusive scenario both partitions are affected by off-shell contributions through non-resonant parts of the gluino propagators, and hence they have their share in the distribution by means of the definition of M_{T2} . To this extent, it was necessary to create a special event sub-sample, which slightly differs from the one introduced in the beginning. With respect to Eq. (6), the factorization of the spectator gluino was exchanged with by full matrix-element calculation according to

$$pp \rightarrow (b\bar{b}\tilde{\chi}_2^0) + (q\bar{q}\tilde{\chi}_1^0) \quad , \quad (20)$$

since the light quarks now also play a role in the construction of M_{T2} . The six-particle final state (with subsequent factorized decay of the second-to-lightest neutralino $\tilde{\chi}_2^0$) is necessary to be able to fully analyze all off-shell effects in this inclusive scenario. The slope parameters in Table 6 confirm the strength of the deviation: while the differences s_d exhibit a significant drop for rising values of γ , the ratios s_r show a minor but steady increase.

In a first summary, mass determination methods generally all suffer from off-shell effects. The amount of smearing in the distribution depends on the exclusiveness or inclusiveness of the variable. In general, the more particles originating from one or even two fat gluinos are involved in the construction of the mass variable, the more distortion or smearing appears in the distributions. The errors in the mass determination already at parton-level can be as large as 10-15 per cent.

4 Effects on Spin Determinations

After a possible discovery of any new physics beyond the SM, the next steps in determining the underlying model characteristics are the measurements of masses and spins of novel particles. While many

mass determinations rely on endpoint positions of invariant mass distributions, the nature of the underlying spin is encoded in the shape of those (and especially angular) distributions and as such more delicate to differentiate. Hence, after discussing the effects of off-shell contributions on mass determination variables, in this section we turn to spin measurements and carefully analyze the effects of a fat gluino onto several methods designed to distinguish a hypothetical SUSY signal from an equivalent one of Universal Extra Dimensions (UED). In general, spin studies compare shapes of distributions by choosing one particular type of mass spectrum which is either of UED or supersymmetric nature. Though typical UED spectra are far more compressed resulting in softer decay products and thus require for more comprehensive analyses (cf. e.g. [25,26]), we choose to stick to hierarchical SUSY like spectra to get a comprehensive comparison. Moreover, as we want to emphasize the difference of spin in intermediate propagators and their impact on invariant mass distributions before comparing it to contributions arising from off-shell effects, we construct a particular UED model, which inherits all masses and width parameters from our SUSY benchmark model and hence allows us to use the particularly interesting decay chain already known from the mass measurement section with the following replacements: $(\tilde{g}, \tilde{b}_i, \tilde{\chi}_2, \tilde{l}_R, \tilde{\chi}_2) \rightarrow (g^{(1)}, b^{(1)}, Z^{(1)}, l^{(1)}, \gamma^{(1)})$. Thus, in this cascade, edges of invariant masses stay the same but shapes thereof are expected to drastically change. In contrast to the gluino, the Kaluza-Klein (KK) gluon will retain a small effective width of $\gamma = 0.5\%$ throughout this analysis. As for the technical side, we use an adapted version of the minimal UED model [27], implemented into WHIZARD using the FEYNRULES [28] interface for WHIZARD [29]. In the sequel, we start to analyze shape asymmetries based on exclusive invariant quark-lepton masses before turning to hadronic correlations inside a single cascade and finally investigating the impact of non-resonant contributions on inclusive angular distributions.

4.1 Shape Asymmetries

Many studies of spin measurements rely on the specific decay topology of the *golden chain* and make inherent use of invariant mass shapes therein as discussed above. Since we are interested in effects emerging from a gluino, we concentrate on an extended version:

$$\tilde{g} \rightarrow q_n \tilde{q}_L \rightarrow q_n q_f \tilde{\chi}_2^0 \rightarrow q_n q_f \ell^\pm \tilde{\ell}_R^\mp \rightarrow q_n q_f \ell^\pm \ell^\mp \tilde{\chi}_1^0 \quad . \quad (21)$$

On the basis of this decay chain, we analyze to what extent the spin determination methods proposed in [26] are affected by the off-shell contributions from a fat gluino. The approaches studied within that paper were designed to discriminate signatures of a supersymmetric gluino from the ones emerging from a Kaluza-Klein gluon excitation in models of UED.

$A^\pm(m_{b\ell})$ At first, we investigate the special bottom-lepton asymmetry with the definition:

$$A^\pm(m_{b\ell}) = \frac{d\sigma/dm_{b\ell^+} - d\sigma/dm_{b\ell^-}}{d\sigma/dm_{b\ell^+} + d\sigma/dm_{b\ell^-}} \quad . \quad (22)$$

We follow the assumptions in [26], namely that the bottom (instead of anti-bottom) quarks are uniquely identified through a lepton charge tag of the b -tagging algorithm. Due to the Majorana nature of the

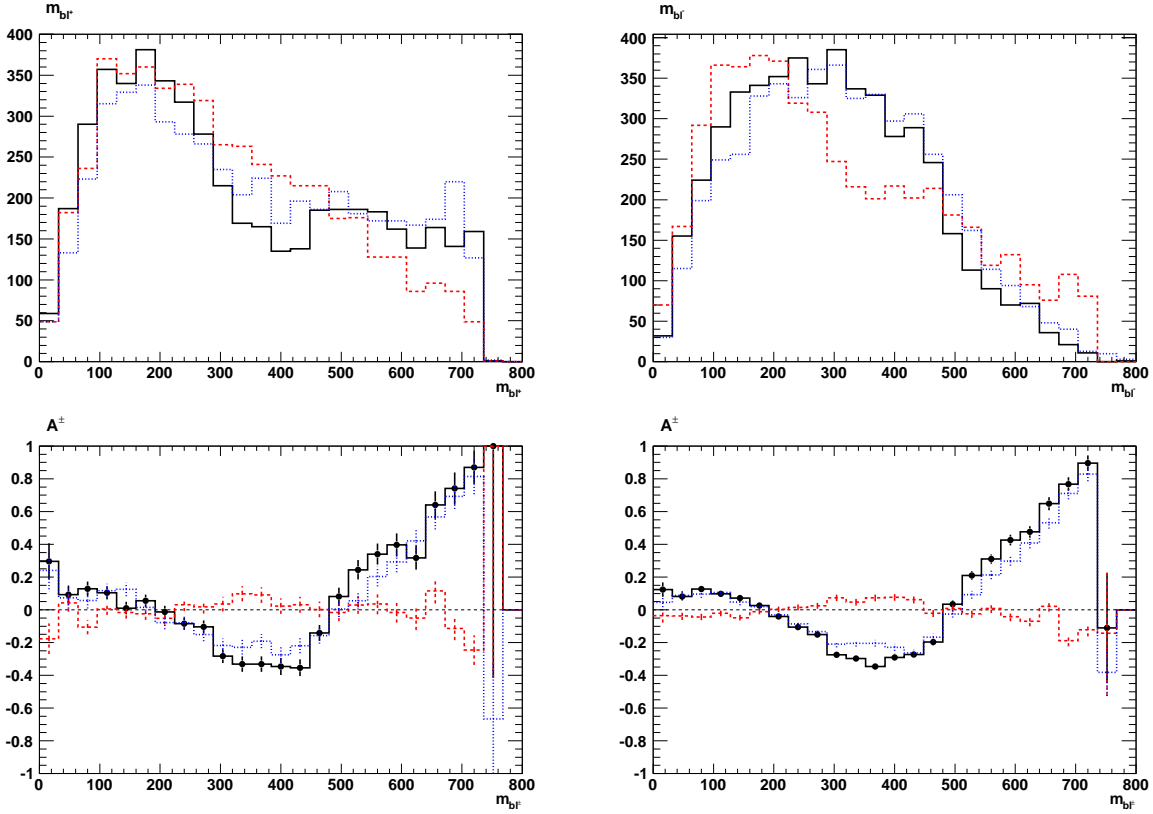


Figure 11: *Invariant masses $m_{b\ell^+}$ (upper left) and $m_{b\ell^-}$ (upper right) with a bottom quark and their asymmetry A^\pm for 5k (lower left) and 25k (lower right) events. The black (solid) and blue (dotted) line correspond to $\gamma = 0.5\%$ and 15.0% , respectively. The UED sample is given by the red (dashed) line.*

gluino, all bottom quarks are near bottom quarks in 50 % of all decays, i.e. they are produced in the first two-body decay step. Hence, visible effects from off-shell contributions of a fat gluino propagator are expected to influence half of the invariant mass shapes. Fig. 11 depicts both the invariant mass distributions of $m_{b\ell^+}$ and $m_{b\ell^-}$ as well as the bottom-lepton asymmetries, for 5k and 25k events. To keep the plots clear and at the same time display all relevant information, we refrain from using all widths, but rather restrict ourselves to the most extreme values of $\gamma = 0.5$ and 15% , given by the black (solid) and blue (dotted) lines as well as the UED sample, depicted by the red (dashed) line.

To clarify whether the deviation of the large-width sample is merely a statistical effect, we artificially increased the event number by a factor of 5 up to 25k. As it turns out in Fig. 11 (on the lower right) there is indeed a subtle effect that is observable in the large width SUSY sample, which is well beyond the size of fluctuations, although both of the two invariant mass distributions show no strong discrepancies with respect to the two different values of γ . Nonetheless, the minimum plateau from 300 to 400 GeV as well as the subsequent rise from 500 to 800 GeV are both reduced by up to one third in magnitude. As is evident through direct comparison with the superimposed UED sample however, it is obvious that large off-shell contributions are not endangering a possible discrimination

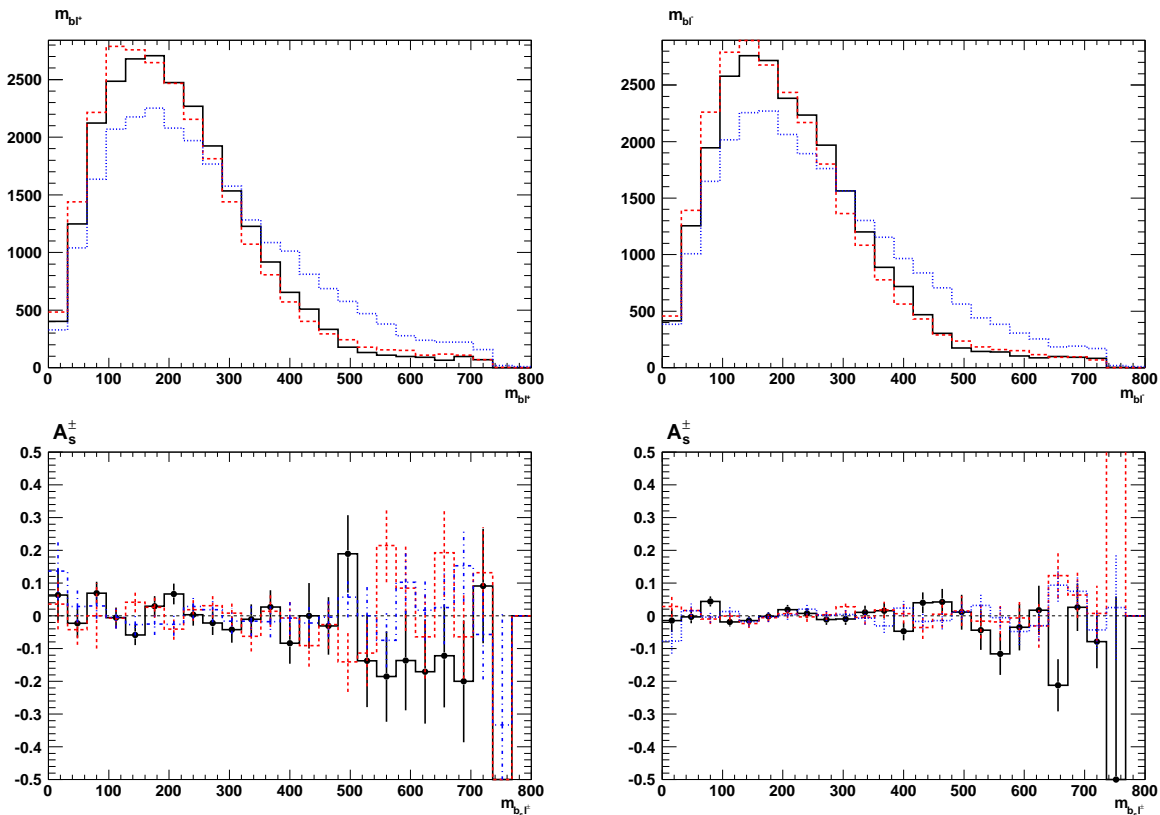


Figure 12: Invariant masses $m_{b_s \ell^+}$ (upper left) and $m_{b_s \ell^-}$ (upper right) with the softer of the two bottom quarks and their asymmetry A_s^\pm for 5k (lower left) and 25k (lower right) events. The color scheme corresponds to the one in Fig. 11

of the fundamentally different spin scenarios, using this specific variable.

$A_s^\pm(m_{b_s \ell})$ Next, we investigate the impact another bottom-lepton asymmetry. The difference to the first asymmetry discussed above is given by the spectrum dependent property that the softer b-quark may coincide with the nearer b-quark. The definition of this asymmetry is given by:

$$A_s^\pm(m_{b_s \ell}) = \frac{d\sigma/dm_{b_s \ell^+} - d\sigma/dm_{b_s \ell^-}}{d\sigma/dm_{b_s \ell^+} + d\sigma/dm_{b_s \ell^-}}. \quad (23)$$

In fact, in our scenario, this assignment is true most of the time: for small width $\gamma = 0.5\%$ in 4557/5000 $\sim 90\%$ of all events, the near bottom quark is also the softer one. Apparently, this changes when the width is increased, as is illustrated in Fig. 1. However, even for the largest width of $\gamma = 15\%$, in 4109/5000 $\sim 80\%$ of all events this assumption is still correct. Obviously, this characteristic will drastically change when the mass gap between the gluino and the sbottom is increased. The nearer quark will become harder due to a larger phase space in the gluino decay, and the value of A_s^\pm will consequently be reduced. In the upper line of Fig. 12 we show both invariant masses, $m_{b_s \ell^+}$ and $m_{b_s \ell^-}$, which exhibit the typical smearing behavior for large widths encountered more often in the

mass measurement section above. Already by eye, the asymmetries in the lower line of Fig. 12 have a comparable pattern: both invariant mass distributions have similar shapes and the corresponding asymmetries are thus rather small. Regardless of the size of the effective width γ , the distortion of $m_{b_s\ell^+}$ mimics the one of $m_{b_s\ell^-}$, and the same holds for the asymmetries. Consequently, the small event sample of 5k is fully compatible with a vanishing asymmetry throughout the complete range of the histogram, not only for the two SUSY samples, but also for UED. Moreover, the larger samples of 25k events also have only minor deviations from $A_s^\pm \equiv 0$, which might be attributed to statistical fluctuations. Altogether, we find the size of this second bottom-lepton asymmetry to be of negligible size compared to the already small deviations found in [26]. Hence, it is not surprising that a steady distortion for both $m_{b_s\ell^+}$ and $m_{b_s\ell^-}$ results in a negligible change of an already very small asymmetry. We conclude that this last asymmetry is neither preferable in terms of discriminative power between SUSY and UED nor for suffering from smearing due to off-shell effects. After all, this should be attributed to the specific kind of underlying mass spectrum.

4.2 Hadronic Angular Correlations

It was further proposed to analyse purely hadronic correlations such as the average pseudo-rapidity $\bar{\eta}_{bb}$ or the difference of azimuthal angles $\Delta\phi_{bb}$ of the two bottom quarks [26]. The first of these

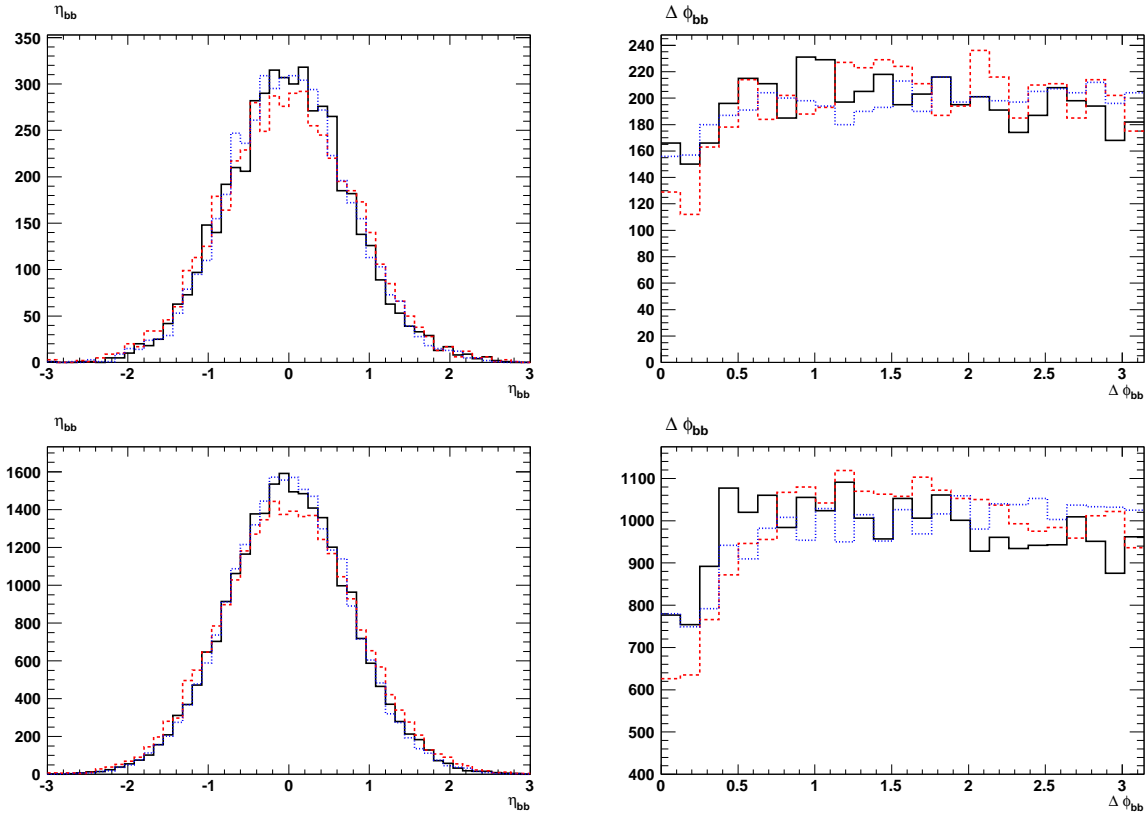


Figure 13: Average pseudo-rapidity (left) and azimuthal distance (right) of both bottom quarks for 5k (top) and 25k (bottom) events. The coloring corresponds to the one in Fig. 11.

observables exhibits no visible distortion with respect to the maximal width γ in the supersymmetric sample, although a small difference to the UED case is perceptible. We confirm the results of [26], where a slightly more central behavior of the two b -quarks was found for SUSY signals. For the azimuthal distance, we find a non-negligible deviation (cf. Fig. 13) of the large width SUSY sample from the standard SUSY sample. In addition, the former turns out to resemble the shape of UED events. As a next step, for each of the two variables the following asymmetries are defined [26]:

$$A_{\eta}^{\pm} = \frac{N(|\bar{\eta}_{bb}| < 1) - N(|\bar{\eta}_{bb}| > 1)}{N(|\bar{\eta}_{bb}| < 1) + N(|\bar{\eta}_{bb}| > 1)} \quad (24)$$

$$A_{\phi}^{\pm} = \frac{N(\Delta\phi_{bb} < \pi/2) - N(\Delta\phi_{bb} > \pi/2)}{N(\Delta\phi_{bb} < \pi/2) + N(\Delta\phi_{bb} > \pi/2)}, \quad (25)$$

which were proposed to obtain an additional measure that allows for a discrimination between a standard SUSY and a UED signal. We apply these variables to our three scenarios, namely the standard and off-shell SUSY as well as the UED samples. Numerical values for all of these are given in Table 7 for 5k and 25k events, respectively. The value of the asymmetry A_{η}^{\pm} of the average

sample	5k	25k
A_{η}^{\pm} (std)	0.627 ± 0.017	0.628 ± 0.008
A_{η}^{\pm} (ofs)	0.645 ± 0.017	0.645 ± 0.008
A_{η}^{\pm} (ued)	0.567 ± 0.016	0.557 ± 0.007
A_{ϕ}^{\pm} (std)	0.014 ± 0.014	0.005 ± 0.006
A_{ϕ}^{\pm} (ofs)	-0.047 ± 0.014	-0.052 ± 0.006
A_{ϕ}^{\pm} (ued)	-0.042 ± 0.014	-0.039 ± 0.006
A_{ct}^{\pm} (std)	0.194 ± 0.015	0.180 ± 0.007
A_{ct}^{\pm} (ofs)	0.125 ± 0.014	0.129 ± 0.006
A_{ct}^{\pm} (ued)	0.003 ± 0.014	0.008 ± 0.006

Table 7: Numerical figures for the three asymmetries A_{ϕ}^{\pm} , A_{η}^{\pm} and A_{ct}^{\pm} defined in equations (25), (24) and (28) for different scenarios: *std*, *ofs* and *ued* correspond to the standard ($\gamma = 0.5\%$) and off-shell ($\gamma = 15\%$) SUSY as well as UED event samples. Errors are purely statistical.

pseudo-rapidity $\bar{\eta}_{bb}$ only exhibits a marginal increase for the off-shell SUSY sample compared to the undistorted standard one. Both coincide within at most two sigma of the purely statistical error. The UED case on the other hand has less central values than the off-shell SUSY parts. This difference to both the standard SUSY sample as well as to the UED sample should be attributed to the fact that the off-shell contributions tend to harden (at least the first) decay product(s) (recall the p_T distributions of the near and far bottom quarks in Figure 1), and hence allow for even more central values of η .

The situation looks a lot less promising for the azimuthal distance $\Delta\phi_{bb}$ of the two bottom quarks. Here, we find that off-shell contributions in the large-width SUSY sample drive the asymmetry A_{ϕ}^{\pm} such that a discrimination between SUSY and UED is no longer possible. Although the shapes of the distributions differ only by a moderate amount visible by eye in all three scenarios (cf. Fig. 13, upper right), the off-shell SUSY sample is washed out in such a way so as to drive the quantitative numerical estimate of the asymmetry negative by the same amount as in the case of UED (cf. Table 7).

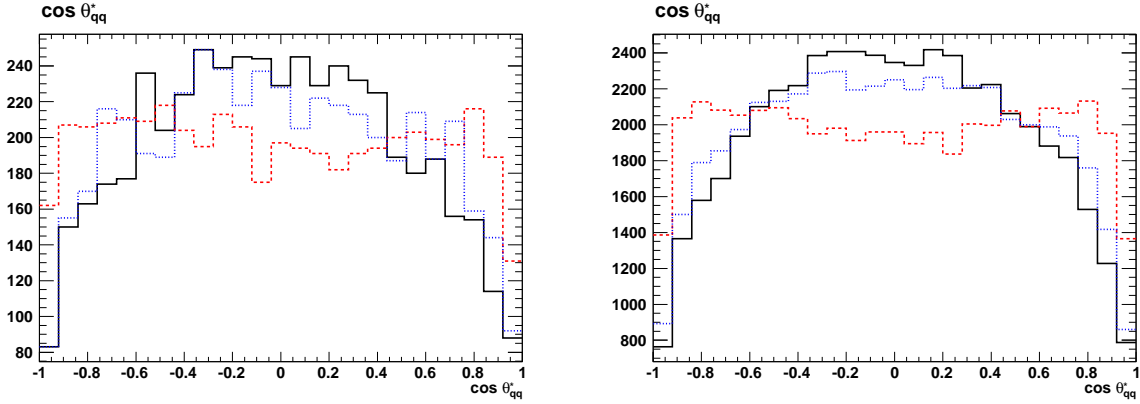


Figure 14: $\cos \theta_{qq}^*$ for 5k (left) and 50k (right) events. The color scheme is the same as in Fig. 11.

4.3 Inclusive Angular Distributions

Finally, we investigate angular correlations of the initially produced particles, which in our case corresponds to gluinos or KK gluons. Although we are not able to reconstruct the complete mother particle momenta due to missing energy, the first emitted partons of each decay cascade should still possess an observable angular correlation among each other. This was first used in the variable

$$\cos \theta_{ll}^* = \tanh \left(\frac{\Delta \eta_{ll}}{2} \right) \quad (26)$$

in a study of slepton pair production [30], and later adapted to general colored SUSY production [31]. The adapted method was applied to fully hadronized inclusive signal event samples with gluino and squark contributions or the corresponding equivalent for UED, where the largest discriminative power is attributed to the squark and KK quark signatures. Our study on the other hand is based on a parton-level analysis, and we restrict ourselves to subsamples with gluinos, since we aim to assess the impact of their off-shell contributions on the method. More precisely, we apply the variable to the *exclusive* gluino benchmark process in our scenario introduced in the beginning in the following way:

$$\cos \theta_{qq}^* = \tanh \left(\frac{\Delta \eta_{q_l q_r}}{2} \right) \quad (27)$$

where $q_l = \min(b_1, b_2)$ and $q_r = \min(q_1, q_2)$ are the softer of the two quarks from each cascade side. While in [31] the largest contributions arise from prompt squark decays to quarks and the lightest neutralinos, and thus $\cos \theta_{qq}^*$ is chosen to be applied to the two hardest objects, we make particular use of the (unfortunately spectrum-dependent) approach of selecting the softer quarks to be attributed to the first (near) gluino or KK-gluon decay products. These are furthermore assumed to inherit features of the initially produced mother particles. Fig. 14 illustrates the behavior of $\cos \theta_{qq}^*$ for the two SUSY scenarios with different widths (black and blue) and the UED scenario (red) for 5k and 50k events, respectively. We included the high statistics sample to show the asymptotic behavior of the fundamentally different models. The distortion due to off-shell contributions is apparent, and although they tend to wash out the distribution to less central values, the differentiation with respect

to UED is not endangered in the exclusive gluino subsample. A quantification of this statement can be obtained through the definition of the following asymmetry [31]:

$$A_{ct}^{\pm} = \frac{N(|\cos \theta_{qq}^*| < 0.5) - N(|\cos \theta_{qq}^*| > 0.5)}{N(|\cos \theta_{qq}^*| < 0.5) + N(|\cos \theta_{qq}^*| > 0.5)}, \quad (28)$$

whose values for the three cases are given in Table 7. The initial observations from Fig. 14 are confirmed: while the value of A_{ct}^{\pm} is indeed reduced by one third in the *standard* SUSY sample with respect to the off-shell SUSY sample, the UED case is compatible with a value of zero. Hence we conclude, that although there is an apparent modification of $\cos \theta_{qq}^*$ due to finite-width effects, it is not threatening the discrimination of SUSY and UED models.

5 Conclusions

In this paper, the impact of off-shell finite-width effects from a broad (“fat”) gluino on a representative selection of observables for mass and spin determination is investigated with a discrete set of effective width-to-mass ratios $\gamma = \Gamma/M \in \{0.5\%, 2.5\%, 5.0\%, 10.0\%, 15.0\%\}$. Such larger widths of gluinos are not uncommon in certain regions of parameter space, and are e.g. quite natural in GMSB scenarios. The basis for this analysis are SUSY signals from gluinos where production and the first decay step are simulated with a full matrix-element calculation to account for non-resonant contributions in the gluino propagator and interferences, distorting kinematic observables. All subsequent decays are then factorized using the NWA, including full spin correlations. An adapted edge-to-bump method is employed to quantify deformations in kinematic distributions, which arise in scenarios with large effective width-to-mass ratios γ . In this approach, several parameters from a naive linear kink function fitted to the corresponding variables are extracted and utilized to quantify errors in the mass and spin determination arising from finite-width effects. In general, mass measurement observables are much more obviously affected in that the endpoint smearing dominates the distributions of otherwise sharp edge structures already at moderate width-to-mass ratios of $\gamma = 5\%$, and steadily increases throughout higher values of γ . As a result, the endpoint positions obtained with the edge-to-bump method are drastically shifted already at the parton level. The difference and the ratio of the two slope parameters in the fit are additional measures of distortion which similarly indicate a washed-out endpoint behavior.

Methods of spin determination are on the other hand less affected by propagator contributions far off the mass-shell. Shape asymmetries as well as angular correlations exhibit only small deviations of event samples with broad gluinos from the ones with a narrow resonance. In the special case of azimuthal distance, the difference of these two event samples however is of considerable size, and although the shapes of the broad SUSY as well as the UED sample still differ, the numerical values of the associated asymmetry A_{ϕ}^{\pm} coincide within their purely statistical errors.

In summary, our studies show that broader BSM resonances as in our case a fat gluino lead to severe distortions of kinematic distributions which are the basis for many mass and spin determination methods. These deviations from non-resonant contributions arise at the fundamental parton level in simulations where production and decay are simulated with the full matrix element. Many existing

studies on the other hand utilise the NWA, whose predictions vigorously differ from the full calculation. Hence a correct treatment of such effects is of crucial importance for both mass and spin measurements so as to not misinterpret the potential signals of much sought-after new physics. While the spin determination might not suffer too much in such cases, broader particles like a fat gluino might make life hard for mass determinations at the LHC.

Acknowledgements

We would like to thank N. Pietsch, K. Rolbiecki, and K. Sakurai for fruitful and enlightening discussions. JRR wants to thank D. Rainwater, who partially initiated the idea for the studies performed here.

References

- [1] D. Berdine, N. Kauer and D. Rainwater, Phys. Rev. Lett. **99**, 111601 (2007) [hep-ph/0703058].
- [2] A. Denner, S. Dittmaier, M. Roth and L. H. Wieders, Phys. Lett. B **612**, 223 (2005) [Erratum-ibid. B **704**, 667 (2011)] [hep-ph/0502063].
- [3] K. Hagiwara *et al.*, Phys. Rev. D **73**, 055005 (2006) [arXiv:hep-ph/0512260].
- [4] J. Reuter, W. Kilian, K. Hagiwara, F. Krauss, S. Schumann, T. Ohl, T. Plehn and D. Rainwater, hep-ph/0512012.
- [5] N. Kauer, JHEP **0804**, 055 (2008) [arXiv:0708.1161 [hep-ph]].
- [6] C. F. Uhlemann and N. Kauer, Nucl. Phys. B **814**, 195 (2009) [arXiv:0807.4112 [hep-ph]].
- [7] B. C. Allanach, M. Battaglia, G. A. Blair, M. S. Carena, A. De Roeck, A. Dedes, A. Djouadi and D. Gerdes *et al.*, Eur. Phys. J. C **25**, 113 (2002) [hep-ph/0202233].
- [8] N. Pietsch, J. Reuter, K. Sakurai and D. Wiesler, JHEP **1207**, 148 (2012) [arXiv:1206.2146 [hep-ph]].
- [9] D. Wiesler, PhD thesis, Hamburg Univ., October 2012.
- [10] J. Reuter and D. Wiesler, Phys. Rev. D **84**, 015012 (2011) [arXiv:1010.4215 [hep-ph]].
- [11] B. Dutta, T. Kamon, N. Kolev and A. Krislock, Phys. Lett. B **703** (2011) 475 [arXiv:1104.2508 [hep-ph]]. A. Rajaraman and F. Yu, Phys. Lett. B **700** (2011) 126 [arXiv:1009.2751 [hep-ph]]; P. Baringer, K. Kong, M. McCaskey and D. Noonan, JHEP **1110** (2011) 101 [arXiv:1109.1563 [hep-ph]]; K. Choi, D. Guadagnoli and C. B. Park, JHEP **1111** (2011) 117 [arXiv:1109.2201 [hep-ph]]; J. Alwall, K. Hiramatsu, M. M. Nojiri and Y. Shimizu, Phys. Rev. Lett. **103** (2009) 151802 [arXiv:0905.1201 [hep-ph]]. M. M. Nojiri and K. Sakurai, Phys. Rev. D **82** (2010) 115026 [arXiv:1008.1813 [hep-ph]].
- [12] A. J. Barr and C. G. Lester, J. Phys. G G **37** (2010) 123001 [arXiv:1004.2732 [hep-ph]]; I. Hinchliffe, F. E. Paige, M. D. Shapiro, J. Soderqvist and W. Yao, Phys. Rev. D **55** (1997) 5520 [hep-ph/9610544]; H. Baer, C. -h. Chen, M. Drees, F. Paige and X. Tata, Phys. Rev. D **59**

- (1999) 055014 [hep-ph/9809223]; I. Hinchliffe and F. E. Paige, Phys. Rev. D **60** (1999) 095002 [hep-ph/9812233]; H. Bachacou, I. Hinchliffe and F. E. Paige, Phys. Rev. D **62** (2000) 015009 [hep-ph/9907518]; I. Hinchliffe and F. E. Paige, Phys. Rev. D **61** (2000) 095011 [hep-ph/9907519]; B. C. Allanach, C. G. Lester, M. A. Parker and B. R. Webber, JHEP **0009** (2000) 004 [hep-ph/0007009]. W. S. Cho, K. Choi, Y. G. Kim and C. B. Park, Phys. Rev. Lett. **100** (2008) 171801 [arXiv:0709.0288 [hep-ph]]; W. S. Cho, K. Choi, Y. G. Kim and C. B. Park, JHEP **0802** (2008) 035 [arXiv:0711.4526 [hep-ph]]; B. Gripaios, JHEP **0802** (2008) 053 [arXiv:0709.2740 [hep-ph]]; A. J. Barr, B. Gripaios and C. G. Lester, JHEP **0802** (2008) 014 [arXiv:0711.4008 [hep-ph]]. M. Burns, K. Kong, K. T. Matchev and M. Park, JHEP **0903** (2009) 143 [arXiv:0810.5576 [hep-ph]]; P. Konar, K. Kong, K. T. Matchev and M. Park, Phys. Rev. Lett. **105** (2010) 051802 [arXiv:0910.3679 [hep-ph]]; T. Cohen, E. Kuflik and K. M. Zurek, JHEP **1011** (2010) 008 [arXiv:1003.2204 [hep-ph]]; A. J. Barr, B. Gripaios and C. G. Lester, JHEP **0911** (2009) 096 [arXiv:0908.3779 [hep-ph]]; P. Konar, K. Kong, K. T. Matchev and M. Park, JHEP **1004** (2010) 086 [arXiv:0911.4126 [hep-ph]]. K. Desch, J. Kalinowski, G. A. Moortgat-Pick, M. M. Nojiri and G. Polesello, JHEP **0402** (2004) 035 [hep-ph/0312069]; K. Kawagoe, M. M. Nojiri and G. Polesello, Phys. Rev. D **71** (2005) 035008 [hep-ph/0410160]; H. -C. Cheng, J. F. Gunion, Z. Han, G. Marandella and B. McElrath, JHEP **0712** (2007) 076 [arXiv:0707.0030 [hep-ph]]; H. -C. Cheng, D. Engelhardt, J. F. Gunion, Z. Han and B. McElrath, Phys. Rev. Lett. **100** (2008) 252001 [arXiv:0802.4290 [hep-ph]]; H. -C. Cheng, J. F. Gunion, Z. Han and B. McElrath, Phys. Rev. D **80** (2009) 035020 [arXiv:0905.1344 [hep-ph]]; B. Webber, JHEP **0909** (2009) 124 [arXiv:0907.5307 [hep-ph]]; M. M. Nojiri, K. Sakurai and B. R. Webber, JHEP **1006** (2010) 069 [arXiv:1005.2532 [hep-ph]].
- [13] S. Chatrchyan *et al.* [CMS Collaboration], arXiv:1211.4784 [hep-ex]; S. Chatrchyan *et al.* [CMS Collaboration], arXiv:1211.3143 [hep-ex]; S. Chatrchyan *et al.* [CMS Collaboration], JHEP **1108** (2011) 155 [arXiv:1106.4503 [hep-ex]]; G. Aad *et al.* [ATLAS Collaboration], arXiv:1211.1167 [hep-ex]. G. Aad *et al.* [Atlas Collaboration], JHEP **1111** (2011) 099 [arXiv:1110.2299 [hep-ex]]; S. Chatrchyan *et al.* [CMS Collaboration], JHEP **1108** (2011) 156 [arXiv:1107.1870 [hep-ex]].
- [14] B. C. Allanach, Comput. Phys. Commun. **143**, 305 (2002) [hep-ph/0104145].
- [15] A. Djouadi, M. M. Muhlleitner and M. Spira, Acta Phys. Polon. B **38**, 635 (2007) [hep-ph/0609292].
- [16] P. Z. Skands, B. C. Allanach, H. Baer, C. Balazs, G. Belanger, F. Boudjema, A. Djouadi and R. Godbole *et al.*, JHEP **0407**, 036 (2004) [hep-ph/0311123].
- [17] B. C. Allanach, C. Balazs, G. Belanger, M. Bernhardt, F. Boudjema, D. Choudhury, K. Desch and U. Ellwanger *et al.*, Comput. Phys. Commun. **180**, 8 (2009) [arXiv:0801.0045 [hep-ph]].
- [18] W. Beenakker, R. Hopker, M. Spira and P. M. Zerwas, Nucl. Phys. B **492** (1997) 51 [arXiv:hep-ph/9610490].
- [19] W. Kilian, T. Ohl and J. Reuter, Eur. Phys. J. C **71** (2011) 1742 [arXiv:0708.4233 [hep-ph]]; M. Moretti, T. Ohl and J. Reuter, arXiv:hep-ph/0102195; W. Kilian, J. Reuter, S. Schmidt and D. Wiesler, JHEP **1204**, 013 (2012) [arXiv:1112.1039 [hep-ph]]; W. Kilian, T. Ohl, J. Reuter and C. Speckner, JHEP **1210**, 022 (2012) [arXiv:1206.3700 [hep-ph]].
- [20] M. Dobbs and J. B. Hansen, Comput. Phys. Commun. **134**, 41 (2001).

- [21] I. Antcheva, M. Ballintijn, B. Bellenot, M. Biskup, R. Brun, N. Buncic, P. .Canal and D. Casadei *et al.*, *Comput. Phys. Commun.* **182**, 1384 (2011).
- [22] D. Curtin, *Phys. Rev. D* **85** (2012) 075004 [arXiv:1112.1095 [hep-ph]].
- [23] C. G. Lester and D. J. Summers, *Phys. Lett. B* **463** (1999) 99 [hep-ph/9906349]; A. Barr, C. Lester and P. Stephens, *J. Phys. G* **29** (2003) 2343 [hep-ph/0304226]; M. M. Nojiri, Y. Shimizu, S. Okada and K. Kawagoe, *JHEP* **0806** (2008) 035 [arXiv:0802.2412 [hep-ph]]; M. M. Nojiri, K. Sakurai, Y. Shimizu and M. Takeuchi, *JHEP* **0810** (2008) 100 [arXiv:0808.1094 [hep-ph]]; S. -G. Kim, N. Maekawa, K. I. Nagao, M. M. Nojiri and K. Sakurai, *JHEP* **0910** (2009) 005 [arXiv:0907.4234 [hep-ph]].
- [24] C. Lester and A. Barr, *JHEP* **0712** (2007) 102 [arXiv:0708.1028 [hep-ph]];
- [25] J. M. Smillie and B. R. Webber, *JHEP* **0510**, 069 (2005) [hep-ph/0507170].
- [26] A. Alves, O. Eboli and T. Plehn, *Phys. Rev. D* **74**, 095010 (2006) [hep-ph/0605067].
- [27] H. -C. Cheng, K. T. Matchev and M. Schmaltz, *Phys. Rev. D* **66**, 056006 (2002) [hep-ph/0205314].
- [28] N. D. Christensen and C. Duhr, *Comput. Phys. Commun.* **180**, 1614 (2009) [arXiv:0806.4194 [hep-ph]].
- [29] N. D. Christensen, C. Duhr, B. Fuks, J. Reuter and C. Speckner, *Eur. Phys. J. C* **72**, 1990 (2012) [arXiv:1010.3251 [hep-ph]].
- [30] A. J. Barr, *JHEP* **0602**, 042 (2006) [hep-ph/0511115].
- [31] G. Moortgat-Pick, K. Rolbiecki and J. Tattersall, *Phys. Lett. B* **699**, 158 (2011) [arXiv:1102.0293 [hep-ph]].